CHALMERS

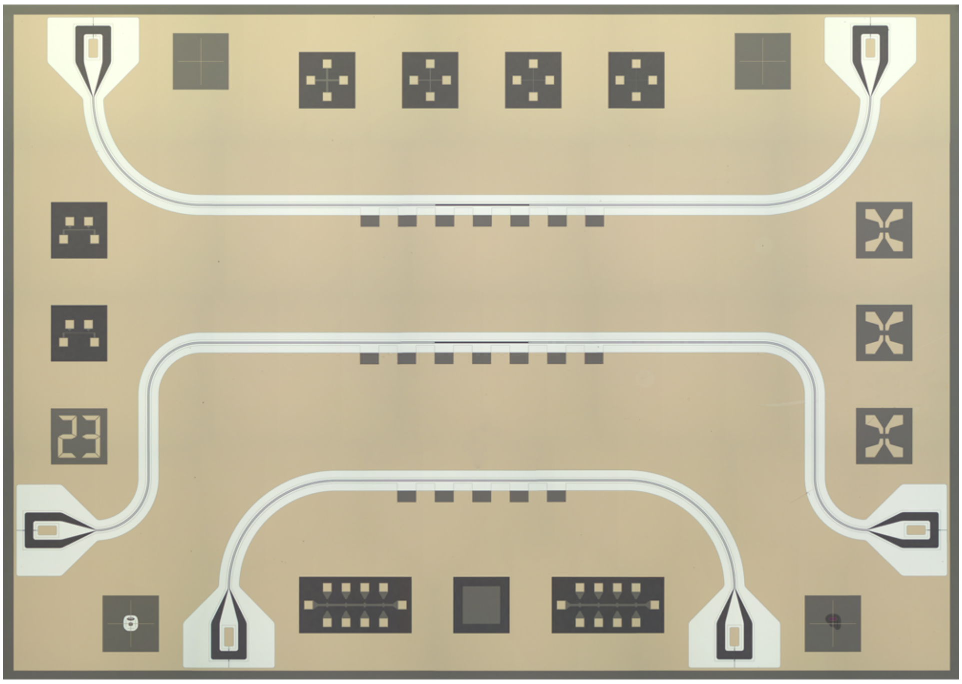

Fabrication and Characterisation of Thin-Film Superconducting Nanowire Superinductors for Novel Quantum Devices

David Niepce

Department of Microtechnology and Nanoscience
Quantum Device Physics Laboratory
CHALMERS UNIVERSITY OF TECHNOLOGY
Göteborg, Sweden 2014

MASTER'S THESIS IN NANOSCIENCE

Fabrication and Characterisation of Thin-Film Superconducting Nanowire Superinductors for Novel Quantum Devices

David Niepce

Department of Microtechnology and Nanoscience
Quantum Device Physics Laboratory
CHALMERS UNIVERSITY OF TECHNOLOGY

Göteborg, Sweden 2014

Fabrication and Characterisation of Thin-Film Superconducting Nanowire Superinductors for Novel Quantum Devices
DAVID NIEPCE

ISSN 1652-8557

Chalmers University of Technology
Department of Microtechnology and Nanoscience
Quantum Device Physics Laboratory
SE-412 96 Göteborg, Sweden
Telephone: +46 (0)31-772 1000

Cover:
One of the chips fabricated and measured during the course of this work. This chip contains two superconducting nanowire superinductances, one 150 nm wide and one 250 nm wide.

Chalmers Reproservice
Göteborg, Sweden 2014

Fabrication and Characterisation of Thin-Film Superconducting Nanowire Superinductors for Novel Quantum Devices
DAVID NIEPCE
Department of Microtechnology and Nanoscience
Chalmers University of Technology, 2014

Abstract

In this master's thesis, we present the design, fabrication and characterisation of superconducting thin-film nanowire superinductances for use in quantum information processing and quantum metrology. In order to characterise the superconducting nanowire, it is placed inside a step-impedance $\lambda/2$ microwave resonator.

In a step-impedance resonator, the strong wave impedance mismatch between the feed lines ($50\,\Omega$) and the nanowire ($\simeq 5\,\mathrm{k}\Omega$) results in the formation of standing waves within the resonator. By measuring the transmission and reflection parameters of the resonator, we can probe the nanowire properties.

We have shown that the high kinetic inductance of thin NbN films can be used to fabricate superinductors that exhibit an inductance two to three orders of magnitude larger than an ordinary geometric inductance of the same size. An inductance of 787 nH is demonstrated for a $200\,\mathrm{nm} \times 1\,\mathrm{mm}$ nanowire. This corresponds to a reactive microwave impedance of $25\,\mathrm{k}\Omega$ at 5 GHz, which is higher than the resistance quantum $h/4e^2 = 6.5\,\mathrm{k}\Omega$.

Keywords: Superconducting circuits, nanowire, superinductance, step-impedance resonator.

Acknowledgements

At the end of this work, I would like to express my gratitude to a number of people who supported me throughout this thesis. First of all I would like to thank my supervisor and examiner Jonas Bylander for giving me such an interesting project, for all his support and confidence in my work and for the countless hours he devoted to me.

I would also like to thank professor Per Delsing and everyone in EMP for welcoming me in the group, for creating such a good atmosphere and work environment and for making me feel at home.

Many thanks to Seçkin Kintas, Sumedh Mahashabde and Philip Krantz for their invaluable help and advices in the cleanroom. I am also grateful toward Henrik Frederiksen, Johan Andersson and the rest of the research and engineering staff of the Nanofabrication Laboratory cleanroom for their help, input and training.

Thanks to Thomas Aref, Ida-Maria Svensson, Maria Ekström, Jeroen Verjauw and of course, Chris Groenveld, for all the good times we spent together in and out of the lab !

Last but not least, I would like to thank my family. Thank you for all your support and for always being there for me. Without you, none of this would have been possible !

David Niepce, October 2014

List of Symbols

Constants		
h	Planck constant	$h \simeq 6.63 \times 10^{-34}\,\mathrm{J\,s}$
$\hbar$	Reduced Planck constant	$h/2\pi \simeq 1.4 \times 10^{-34}\,\mathrm{J\,s}$
e	Elementary charge	$e \simeq 1.6 \times 10^{-19}\,\mathrm{C}$
c	Speed of light in vacuum	$c \simeq 3 \times 10^{8}\,\mathrm{m/s}$
k_B	Boltzmann's constant	$k_B \simeq 1.4 \times 10^{-23}\,\mathrm{J/K}$
μ_0	Vacuum permability	$4\pi \times 10^{-7}\,\mathrm{Vs/Am}$
ϵ_0	Vacuum permittivity	$8.85 \times 10^{-12}\,\mathrm{F/m}$
R_K	Von Klitzing constant	h/e^2
R_Q	Superconducting resistance quantum	$h/4e^2 \simeq 6.5\,\mathrm{k\Omega}$
α	Fine structure constant	$c\mu_0/2R_K \simeq 1/137$

Chapter 1: Introduction	
L	Inductance per length of the wire
C	Capacitance per length of the wire

Chapter 2: Theoretical Background	
ψ_S	Superconducting wave function
Φ	Quantum mechanical phase
Δ	Superconducting gap
λ_L	London penetration depth
τ	Average time between scattering events (Drude model)
δ	Skin depth in a normal metal
Z_S	Surface impedance of a superconducting film
L_k	Kinetic inductance of a superconducting strip
L_m	Magnetic inductance of a superconducting strip
ξ_0	BCS coherence length
v_f	Fermi velocity
R_N	Normal state resistance
Z_0	Characteristic impedance
Z_0'	Characteristic impedance
γ	Propagation constant
C_s	Shunt capacitance
S_{11}	Reflection parameter
S_{21}	Transmission parameter

Chapter 3: Experimental Techniques	
λ_e	de Broglie wavelength for electrons
p_e	momentum of electrons
t_{acc}	Spinner acceleration time

Chapter 4: Results and Discussion

R_{RMS}	Root mean squared roughness
R_{sk}	Skewness
R_{ku}	Kurtosis
P_c	Critical input power
I_c	Critical current
j_c	Critical current density

List of Figures

List of Tables

Contents

Chapter 1

Introduction

In the early 1990s, the concept of solving problems with the use of quantum algorithms was proposed. This was the starting point of the quest for the so-called *quantum computer* where a quantum bit (*qubit*) is a unit of quantum information (the quantum analogue of the classical bit) and takes advantage of the superposition principle: a qubit can be in two states simultaneously. Since then, Quantum Information Processing (QIP) has become a rapidly developing field of research spanning both physics and computer science [1, 2]. Multiple implementations of qubits have been developed, ranging from the polarisation of photons to spins of the nucleus of atoms and microfabricated structures such as quantum dots or superconducting loops. However, while tremendous progress has been made, decoherence of the quantum states due to noise is still a major problem.

Josephson junction-based qubits constitute a promising platform for QIP [3]. By embedding a Josephson junction in a high impedance environment, we can effectively suppress charge fluctuations. According to the Heisenberg principle[1], in order to reduce the charge fluctuations across the Josephson junction below $2e$, the impedance must be larger than the superconducting resistance quantum $R_Q = h/4e^2 \simeq 6.5\,\mathrm{k\Omega}$.

This cannot be achieved by ordinary *geometric* inductances: any finite-length wire comes with a self-capacitance which reduces the total charging energy of the circuit unless $\sqrt{L/C} \gg R_Q$. A purely electromagnetic inductance is incompatible with such a requirement as it is in practice always bounded by the vacuum impedance $\sqrt{\mu_0/\epsilon_0} \simeq 377\,\Omega < R_Q$. This is related to the fine structure constant α characterising the strength of the electromagnetic interaction between elementary charged particles: $\alpha = c\mu_0/2R_K = \sqrt{\mu_0/\epsilon_0}/8R_Q \simeq 1/137 \ll 1$. This limitation, however, can be beaten by taking advantage of superconducting circuits. The *kinetic inductance* associated with the inertia of the Cooper pairs can be very high, allowing the realisation of *superinductances* [4].

Moreover, in Quantum Metrology, the *quantum metrology triangle* [5] reflects the fundamental relationships between the basic electrical quantities, namely the voltage, current and frequency, given by quantum mechanical laws. Two sides of the triangle already have practical realisations:

[1]The phase operator $\hat{\Phi}$ and the charge operator $\hat{Q} = -i\hbar\partial/\partial\Phi$ are canonical conjugates and $[\hat{\Phi}, \hat{Q}] = i\hbar$

the voltage standard is realised by locking the oscillations of the Josephson current to an external radiation of frequency f, leading to Shapiro steps at voltages $V_n = nfh/2e, n \in \mathbb{N}$. Voltage is related to current with the quantum Hall effect where $V_n = (nh/e^2)I$. However, a current standard has yet to be realised.

Superinductors are ideal to apply a well-defined current bias across a Josephson junction. A direct current would flow by the passage of single Cooper pairs, which can be locked to produce dual Shapiro steps at the currents $I_n = nf2e$. This would constitute a current standard and effectively provide the missing third side of the triangle.

Recently, superinductors have been realised using Josephson junction arrays and were succesfully used to demonstrate noise-protected qubits [6, 7, 8]. We intend to take the alternative approach, suggested by A. J. Kerman [9], and build superinductors by using the kinetic inductance of very thin-film superconducting nanowires.

In this work, we present the design, fabrication and characterisation of NbN superconducting nanowire superinductors.

Chapter 2

Theoretical Background

2.1 Superconductivity

On April 8, 1911, while studying the resistance of solid mercury at cryogenic temperatures using liquid helium as refrigerant, Heike Kamerlingh Onnes observed that the resistance abruptly disappeared below a critical temperature T_c of 4.2 K [10]. This phenomenom, now known as *superconductivity*, was observed in several other materials such as lead, in 1913, ($T_c = 7\,\mathrm{K}$) or niobium nitride, in 1941 ($T_c = 16\,\mathrm{K}$).

A theory explaining this behaviour and many other properties of superconductors was proposed by Bardeen, Cooper and Schrieffer, who in 1957 showed that the interractions between the electrons in the metal and the vibrations of its atom lattice (phonons) give rise to an attractive force between the electrons overcoming the Coulomb repulsion. It becomes energetically favourable for the electrons to form pairs [11]. While an electron is a fermion, the electron pairs, known as *Cooper pairs*, are bosons and are therefore not subject to the Pauli exclusion principle. The superconducting state of a metal appearing at very low temperature, almost all the Cooper pairs will be bound to stay in their lowest energy state: the Cooper pairs condensate into a single ground state Ψ_S

$$\Psi_S = \sqrt{n_s} e^{i\phi} \tag{2.1}$$

where n_s is the density of Cooper pairs and ϕ the quantum mechanical phase.

Superconductors exhibit a number of common properties. First of all, when the superconducting phase transition occurs ($T < T_c$), electrons around the Fermi energy condense into Cooper-pairs and leave an energy gap Δ in the electronic band structure of the material. As long as the thermal energy is less than the superconducting gap Δ (also known as the *binding energy*), the Cooper pairs are not scattered and current can flow without any resistance: superconductors have a zero electrical DC resistance. At $T = 0$, the superconducting gap can be expressed as

$$2\Delta \simeq 3.5 k_B T_c \tag{2.2}$$

Another major property, called the Meissner effect [12], describes the expulsion of a magnetic field from a superconductor during its transition to the superconducting state. External magnetic fields generate circulating currents near the surface of the superconductor via induction (Eddy currents). In turn, these currents generate a magnetic field opposite to the external field thus cancelling any field inside the superconductor. A classical approach of this phenomenon by F. and H. London [13] showed that any external field is exponentially screened inside the superconductor with a characteristic distance λ_L known as the *London penetration depth*

$$\lambda_L = \sqrt{\frac{m}{\mu_0 n_s e^2}} \tag{2.3}$$

where n_s is the density of Cooper pairs and m and e are respectively the mass and charge of an electron.

2.2 Kinetic Inductance

Kinetic inductance is the manifestation of the inertial mass of mobile charge carriers in alternating electric fields as an equivalent series inductance. Kinetic inductance is observed at very high frenquencies in high carrier mobility conductors and superconductors.

2.2.1 The Conductivity of Normal Metals

The conductivity of a normal metal can be derived using the Drude model where an electric field is applied to an electron gas [14]. The electrons respond to the field by being accelerated and gaining momentum until they scatter off an ion and are given some new random direction and velocticy. The scattering process is characterised by an average time τ between scattering events and over many scattering events, the electrons will have some average momentum in the direction of the field. The derivation of the Drude model leads to the following expression for the conductivity

$$\sigma_n = \sigma_{1n} - i\sigma_{2n} = \frac{n_n e^2 \tau}{m(1+\omega^2\tau^2)} - i\frac{n_n e^2 \omega \tau^2}{m(1+\omega^2\tau^2)} \tag{2.4}$$

where m is the effective electron mass and n_n the electron density.

However, in normal metals, the collision time is typically $\tau \simeq 1 \times 10^{-14}\,\mathrm{s}$. Therefore for frequencies $< 100\,\mathrm{GHz}$, the term $\omega^2\tau^2$ is very small and can be ignored.

2.2.2 The Two-Fluid Model

In 1934, Gorter and Casimir proposed the *two-fluid model* [15] to describe the electrodynamics of a superconductor at a finite temperature: when the superconductor undergoes its transition into the superconducting state ($T < T_c$) the population of electrons is divided in two parts. One population of density n_n consists of normal single electrons, known as quasi-particles, subject to scattering and thus exhibiting losses. The other population of density n_s consists of electrons paired in Cooper pairs, immune to scattering effects hence exhibiting no loss. In this model, the current in a superconductor follows two paths: one path through the superconducting electrons paired up in Cooper pairs (n_s) and through normal electrons (n_n). The total number of conducting electrons in the material is given by $n = n_s + n_n$ and the ratio n_s/n is given by

$$\frac{n_s}{n} = 1 - \left(\frac{T}{T_c}\right)^4 \tag{2.5}$$

The temperature dependance of n_s means that the London penetration depth also depends on temperature leading to the expression

$$\lambda_L(T) = \lambda_L(0)\left[1 - \left(\frac{T}{T_c}\right)^4\right]^{-1/2} \tag{2.6}$$

where $\lambda_L(0) = \sqrt{m/\mu_0 e^2 n}$ is the London penetration depth at $0\,\mathrm{K}$ ($n_s = n$ at $0\,\mathrm{K}$).

The conductivity σ_n of the normal electrons is described by equation 2.4. The superconducting electrons do not scatter, therefore by taking $\tau \to \infty$, equation 2.4 leads to the conductivity σ_s of the superconducting electrons

$$\sigma_s = -i\frac{n_s e^2}{\omega m} \tag{2.7}$$

This leads to the general expression of the conductivity for a superconductor in the two-fluid model

$$\sigma = \frac{n_n e^2 \tau}{m(1+\omega^2\tau^2)} - i\left(\frac{n_n e^2 \omega \tau^2}{m(1+\omega^2\tau^2)} + \frac{n_s e^2}{\omega m}\right) \tag{2.8}$$

In the DC regime ($\omega = 0$), the conductivity is purely imaginary and accounts for the zero resistance effect that made superconductors famous. However, as we move to higher temperatures or frequencies, an increase of σ_n along with the decrease of σ_s means that a larger fraction of the current is shunted through the resistive path compared to lower temperatures or frequencies: the superconductor will exhibit losses as the temperature or frequency increases. Moreover, the inertia of the superconducting electrons produces a reactance leading to a large impedance at high frequencies: this is the *kinetic inductance*. Figure 2.1 gives a schematic representation of the two current paths.

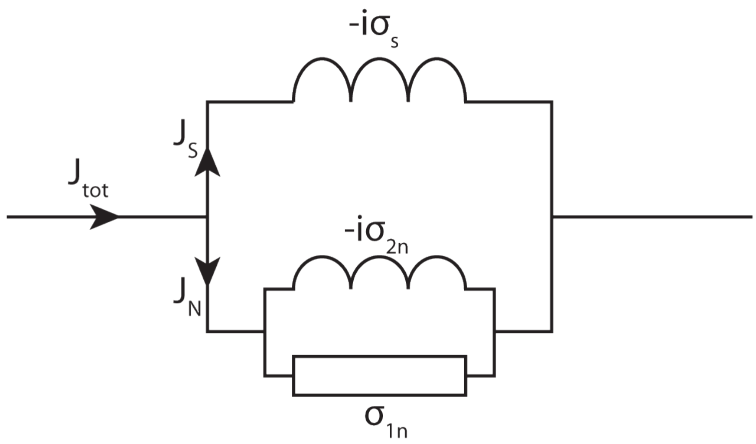

Figure 2.1: Two-fluid model current paths equivalent circuit. The supercurrent path takes the form of an inductance with zero loss. The normal electrons current path takes the form of a resistive path in parallel with an inductive path accouting for both the real (σ_{1n}) and imaginary components (σ_{2n}) of the normal conductivity.

In the microwave regime, where $\omega\tau \ll 1$, equation 2.8 can be simplified into

$$\sigma = \sigma_1 - i\sigma_2 = \frac{n_n e^2 \tau}{m} - i\frac{n_s e^2}{\omega m} \tag{2.9}$$

where σ_1 accounts for the conductivity of normal electrons and σ_2 for the superconducting electrons. Moreover, since for $T > T_c$ all electrons are in the normal state, we have

$$n_n = n \text{ and } \sigma = \sigma_n = \frac{ne^2\tau}{m} \tag{2.10}$$

In the same way, at $T = 0\,\mathrm{K}$, all the electrons are in the superconducting state, we have

$$n_s = n \text{ and } \sigma = \sigma_s = \frac{ne^2}{\omega m} = \frac{1}{\mu_0 \omega \lambda_L^2(0)} \tag{2.11}$$

leading to

$$\sigma = \frac{n_n}{n}\sigma_n - i\frac{1}{\mu_0 \omega \lambda_L^2(T)} \tag{2.12}$$

2.2.3 Surface Impedance of a Superconductor

In most cases, the complex conductivity is not accessible experimentally and instead the complex surface impedance $Z_S = R_S + iX_S$, defined as the ratio of the electromagnetic electric field over the magnetic field at the surface, is the quantity being probed.

It is well known that an electromagnetic field penetrates into a normal metal with a finite skin depth δ. The skin depth can be calculated using Maxwell's equations and the local Ohm's law $\vec{J}_n(\vec{r}) = \sigma_n \vec{E}(\vec{r})$. We have

$$\delta = \sqrt{\frac{2}{\mu_0 \omega \sigma}} \tag{2.13}$$

This skin depth implies that the in-plane electromagnetic field components will decay exponentially inside the conductor. We can therefore write, for the electric field in the conductor:

$$E_x(z) = E_x(0) e^{-\frac{z}{\delta}(1+i)} \tag{2.14}$$

And by applying the Maxwell-Faraday equation, an expression for the magnetic field immediately follows

$$H_y(z) = \frac{1-i}{\mu_0 \omega \delta} E_x(z) \tag{2.15}$$

This finally leads to

$$Z_S = \frac{E_x(0)}{H_y(0)} = \sqrt{\frac{i\omega\mu_0}{\sigma}} \tag{2.16}$$

In a similar way, due to the Meissner effect, an electromagnetic field penetrates over the London penetration depth λ_L in a superconductor. It has been shown that the normal metal approach still holds for a superconducting film in the local limit [16]. By inserting equation 2.12 into 2.16, we can derive an expression for the surface impedance in the two-fluid model

$$Z_S = \sqrt{\frac{i\omega\mu_0}{\sigma_1 - i\sigma_2}} \simeq \frac{1}{2}\omega^2 \mu_0^2 \lambda_L^3(T)\sigma_1 + i\omega\mu_0\lambda_L(T) \tag{2.17}$$

To emphasise the frequency and temperature dependence of the inductive component of this impedance $X_S = \omega\mu_0\lambda_L(T)$, we can rewrite it as

$$X_S(\omega, T) = \sqrt{\frac{\frac{\mu_0 \omega}{\sigma_2(\omega,T)}}{1 - \left(\frac{T}{T_c}\right)^4}} \tag{2.18}$$

For the case of a very thin superconducting film ($t \ll \lambda_L$), the mean free path of the electrons is limited by t. The main losses are due to surface scattering and the current density can be considered as homogeneous in the entire film cross section. It has been shown [17] that the surface impedance can then be reduced to

$$Z_S = \frac{1}{t(\sigma_1 - i\sigma_2)} \tag{2.19}$$

2.2.4 Internal Inductance

In a superconducting strip, energy can be stored in two different ways. One part is stored in the classical magnetic energy E_{mag} due to the magnetic field induced by the applied current. This energy depends on the geometry of the conductor and is given by

$$E_{mag} = \int \frac{\mu_0 \vec{H}^2}{2} dV = \frac{1}{2} L_m I^2 \tag{2.20}$$

where L_m is the magnetic inductance consisting of $L_m = L_{m,int} + L_{m,ext}$. $L_{m,int}$ is the inductance due to the magnetic field that penetrates into the superconductor with over λ_L and $L_{m,ext}$ is the inductance arising from the magnetic field around the conductor, defined by the length and the cross section of the conductor.

A second part of the energy is associated with the kinetic energy of the superconducting electrons. We can write the kinetic energy E_{kin} of the Cooper pairs using $J_s = n_s e v$

$$E_{kin} = \int \frac{m n_s v}{2} dV = \frac{m}{2 n_s e^2} \int J_s^2 dV = \frac{1}{2} L_k I^2 \tag{2.21}$$

where v is the average velocity of the charge carriers and L_k is the *kinetic inductance*. We can see from this last equation that an increase in density of Cooper pairs n_s leads to a decrease of the kinetic energy, reaching a minimum at $T = 0\,\mathrm{K}$. By increasing the temperature, Cooper pairs break up into normal electrons leading to a decrease of n_s and σ_2 and an increase of n_n and σ_1. A lower Cooper pair density forces the Cooper pairs to increase their velocity in order to provide the same supercurrent J_s. This means that the reactive part of the surface impedance Z_S increases due to the inertia of the Cooper pairs, giving rise to the kinetic inductance L_k.

Expressions for both the kinetic inductance L_k and the magnetic inductance $L_{m,int}$ have been derived [18] in the general case for a superconducting strip of width W and read as

$$L_k = \frac{\mu_0 \lambda_L}{4W} \left[\coth\left(\frac{t}{2\lambda_L}\right) + \left(\frac{t}{2\lambda_L}\right) \mathrm{cosec}^2\left(\frac{t}{2\lambda_L}\right) \right] \tag{2.22}$$

$$L_{m,int} = \frac{\mu_0 \lambda_L}{4W} \left[\coth\left(\frac{t}{2\lambda_L}\right) - \left(\frac{t}{2\lambda_L}\right) \mathrm{cosec}^2\left(\frac{t}{2\lambda_L}\right) \right] \tag{2.23}$$

Leading to the following expression for the total internal inductance

$$L_{int} = L_{m,int} + L_k = \frac{\mu_0 \lambda_L}{4W} \coth\left(\frac{t}{2\lambda_L}\right) \tag{2.24}$$

As we can see in figure 2.2, in the case of a very thin film ($t \ll \lambda_L$), the geometric contribution to the total inductance is completely negligible and we have

$$L = L_k = \frac{\mu_0 \lambda_L^2}{W t} \tag{2.25}$$

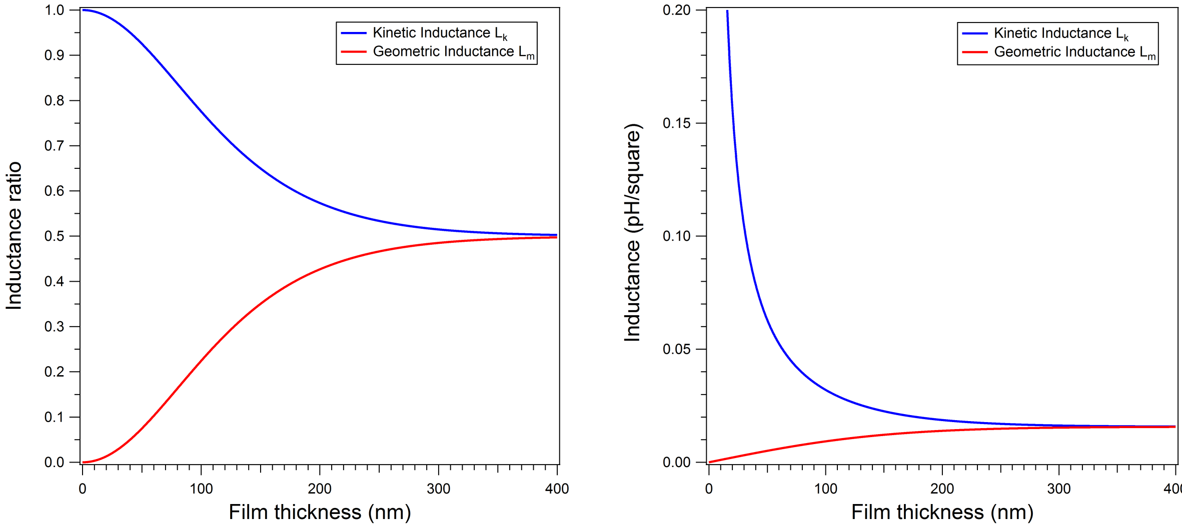

Figure 2.2: (Left) Ratios of $L_{m,int}$ and L_k to the total internal inductance. (Right) $L_{m,int}$ and L_k in pH per Square. This demonstrates a large increase in kinetic inductance as the film thickness decreases. Both plots created for $\lambda_L = 50\,\mathrm{nm}$

Taking this into consideration, the surface impedance for thin superconducting films can be expressed by

$$Z_S = R_S + iX_S = R_S + i\omega L_k \tag{2.26}$$

By using this expression and equation 2.19, this leads to the following expression for the kinetic inductance in pH/square

$$L_k = \frac{\sigma_2}{t\omega(\sigma_1^2 + \sigma_2^2)} \tag{2.27}$$

2.2.5 The Mattis-Bardeen Theory

The results based on London's equations and the two-fluid model derived in the previous sections hold remarkably well but are not derived from any fundamental principle of superconductivity and do not take into account the idea of a band gap. Moreover, the London model does not take into account the finite size of a Cooper pair: the interaction between electrons forming a Cooper pair happens over an average distance known as the *coherence length* ξ. In the BCS microscopic theory of superconductivity, the coherence length is given by

$$\xi_0 = \frac{0.18\hbar v_f}{k_B T_c} \tag{2.28}$$

The coherence length in a typical superconductor is of the order of 1 µm. This distance being much larger than the electron spacing, it becomes clear that a non-local[1] treatment is necessary. This was suggested by Pippard [19] using similarities in the non-local theory for Ohm's law in rapidly varying spatial electric fields (the so-called anomalous skin effect in metals) and the second London equation. The effects on the band gap and the non-local treatment of Cooper pairs leads to the Mattis-Bardeen equations [20] for the complex conductivity $\sigma(\omega) = \sigma_1 - i\sigma_2$ relative to the normal state conductivity σ_n, assuming the extreme anomalous limit $\lambda_L \ll \xi$[2]:

$$\frac{\sigma_1(\omega)}{\sigma_n} = \frac{2}{\hbar\omega}\int_{\Delta}^{\infty} dE \frac{E^2 + \Delta^2 + \hbar\omega E}{\sqrt{E^2 - \Delta^2}\sqrt{(E + \hbar\omega)^2 - \Delta^2}}(f(E) - f(E + \hbar\omega)) \tag{2.29}$$

$$\frac{\sigma_2(\omega)}{\sigma_n} = \frac{2}{\hbar\omega}\int_{\Delta}^{\Delta+\hbar\omega} dE \frac{E^2 + \Delta^2 - \hbar\omega E}{\sqrt{E^2 - \Delta^2}\sqrt{\Delta^2 - (E - \hbar\omega)^2}}(1 - 2f(E)) \tag{2.30}$$

where f is the Fermi-Dirac distribution function $f(E) = 1/(1 + \exp(E/k_B T))$. At low temperatures where $T \ll T_c$, σ_1 will vanish and we can rewrite σ_2 as

$$\frac{\sigma_2}{\sigma_n} = \frac{\pi\Delta_0}{\hbar\omega}\left[1 - \frac{1}{16}\left(\frac{\hbar\omega}{\Delta_0}\right)^2 - \frac{3}{1024}\left(\frac{\hbar\omega}{\Delta_0}\right)^4 + ...\right] \tag{2.31}$$

Since σ_1 vanishes at very low temperatures by using a sufficiently low temperature one can make the microwave dissipation of a superconductor arbitrary low: the dissipative response of the electron system becomes very small compared to the reactive response ($\sigma_1 \ll \sigma_2$). In the limit that the film is thin compared to its London penetration depth ($t \ll \lambda_L$), we can use these results in equation 2.27. A first order development (in σ_1/σ_2) leads to

$$L_k = \frac{\sigma_2}{t\omega(\sigma_1^2 + \sigma_2^2)} = \frac{\sigma_2}{t\omega\sigma_2^2(1 + (\sigma_1/\sigma_2)^2)} \simeq \frac{1}{t\omega\sigma_2} = \frac{\hbar}{\pi\Delta_0 t\sigma_n} = \frac{\hbar R_N}{\pi\Delta_0} \tag{2.32}$$

where $R_N = 1/(\sigma_n t)$ represents the normal state sheet resistance of our film.

2.3 Microwave Transmission Lines

The transmission lines used in this work are Coplanar Waveguides (CPW) originally described by C. P. Wen [21]. Like in a coaxial cable, the propagating microwave photons in the line give rise to Transverse Electromagnetic (TEM) waves. The properties of the transmission line can be studied by the telegraph equations [22] where the transmission line is represented by a succession of infinitesimally short segments of length dz as pictured in figure 2.3. The voltage and current can be written as

$$\begin{cases} V(z) = V^+ e^{-\gamma z} + V^- e^{\gamma z} \\ I(z) = I^+ e^{-\gamma z} + I^- e^{\gamma z} \end{cases} \tag{2.33}$$

[1] In physics, non-locality or "action at a distance" is the direct interaction of two objects that are separated in space with no perceivable intermediate agency or mechanism.

[2] See section 4.3 for a discussion about whether or not this hypothesis holds for our devices.

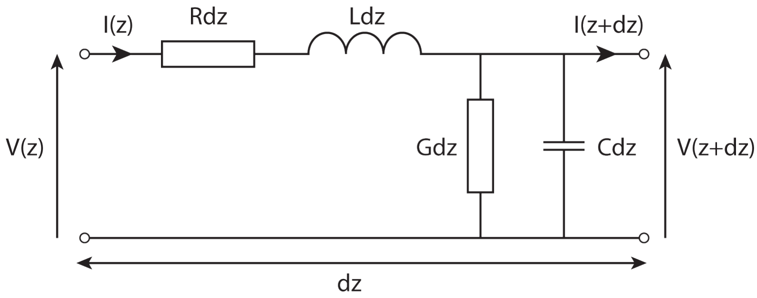

Figure 2.3: Lumped element representation of a segment of length dz of a transmission line with the resistance R, inductance L, capacitance C and shunt conductance G per unit length.

where $\gamma = \alpha + i\beta = \sqrt{(R + i\omega L)(G + i\omega C)}$ is the complex propagation constant. From these, the characteristic impedance and ABCD matrix (see derivation of the ABCD matrix in appendix C) of the line follow

$$Z_0 = \frac{V^+}{I^+} = -\frac{V^-}{I^-} = \sqrt{\frac{R + i\omega L}{G + i\omega C}} \tag{2.34}$$

$$ABCD(l) = \begin{pmatrix} \cosh(\gamma l) & Z_0 \sinh(\gamma l) \\ 1/Z_0 \sinh(\gamma l) & \cosh(\gamma l) \end{pmatrix} \tag{2.35}$$

where l represents the length of the line.

For a superconducting transmission line with very small losses, we can neglect R and G and therefore rewrite the previous expressions as

$$\gamma = i\beta = i\omega\sqrt{LC} \tag{2.36}$$

$$Z_0 = \sqrt{\frac{L}{C}} \tag{2.37}$$

$$ABCD(l) = \begin{pmatrix} \cos(\beta l) & Z_0 \sin(\beta l) \\ 1/Z_0 \sin(\beta l) & \cos(\beta l) \end{pmatrix} \tag{2.38}$$

2.4 Stepped Impedance Coplanar Resonator

The step change in the central strip conductor of a coplanar waveguide perturbs the normal CPW electric and magnetic fields and gives rise to additional reactances. The step discontinuity is generally modeled by a shunt capacitor C_s as presented in appendix D. We can therefore express the ABCD matrix of the step discontinuity as

$$ABCD_{step} = \begin{pmatrix} 1 & 0 \\ iC_s\omega & 1 \end{pmatrix} \tag{2.39}$$

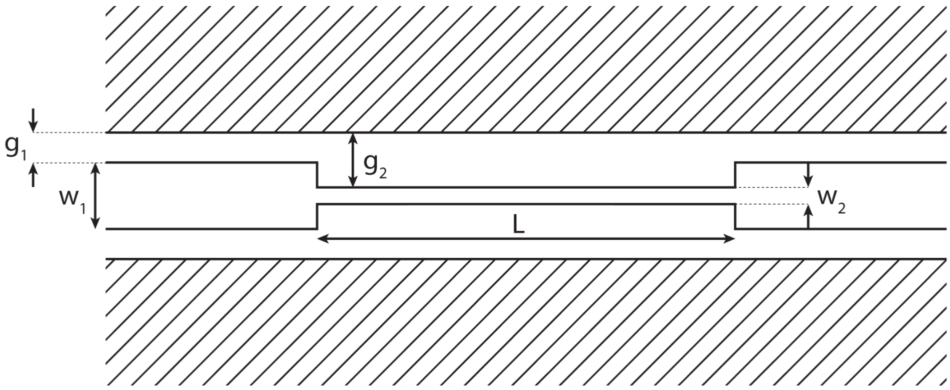

Figure 2.4: A stepped impedance coplanar resonator. A strip of length l and width w_2 is placed inside a coplanar waveguide with a conductor width $w_1 > w_2$. The impedance mismatch at the steps allows the formation of standing waves in the central area, forming a resonator.

By placing two symetrical step discontinuities as shown in figure 2.4, the impedance mismatch at the steps allows the formation of standing waves in the central area: we form a resonator. The stepped impedance coplanar resonator can be seen as a transmission line of characteristic impedance Z_0' different than Z_0, the characteristic impedance of the feed line, as shown in figure 2.5.

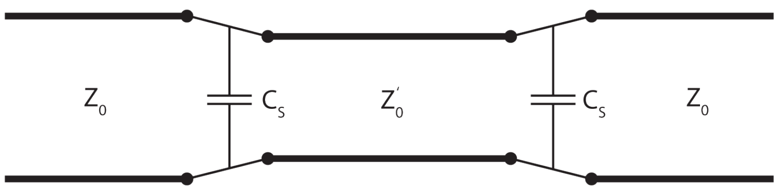

Figure 2.5: Equivalent circuit for a stepped impedance coplanar resonator. The resonator is considered as a transmission line of characteristic impedance Z_0' and length l placed inside a feed line of characteristic impedance Z_0. The steps in the width of the central conductor strip are modeled by a shunt capacitor C_s.

Assuming lossless transmission lines, the total ABCD matrix of the resonator can be expressed by

$$\begin{aligned} ABCD &= \begin{pmatrix} A & B \\ C & D \end{pmatrix} = ABCD_{step} \times ABCD_{strip} \times ABCD_{step} \\ &= \begin{pmatrix} 1 & 0 \\ iC_s\omega & 1 \end{pmatrix} \begin{pmatrix} \cos(\beta l) & Z_0' \sin(\beta l) \\ 1/Z_0' \sin(\beta l) & \cos(\beta l) \end{pmatrix} \begin{pmatrix} 1 & 0 \\ iC_s\omega & 1 \end{pmatrix} \end{aligned} \tag{2.40}$$

From the elements of the ABCD matrix, we can express the S-parameters of our resonator [23]. We retain the expressions of both the reflection (S_{11}) and transmission (S_{21}) coefficients

$$S_{11} = \frac{A + B/Z_0 - CZ_0 - D}{A + B/Z_0 + CZ_0 + D} \tag{2.41}$$

$$S_{21} = \frac{2}{A + B/Z_0 + CZ_0 + D} \tag{2.42}$$

2.5 Superconducting Nanowire Superinductance

We showed that a very thin superconducting film will have a very high sheet kinetic inductance. Therefore, by replacing the conductor strip of our stepped impedance coplanar resonator by a *superconducting nanowire*, a narrow wire etched in the very thin superconducting film, a very high kinetic inductance is obtained in the central strip, leading to a high impedance mismatch in the resonator: the feed lines have a characteristic impedance of $Z_0 = 50\,\Omega$, however the characteristic impedance of the nanowire Z_0' will be of the order of a few kΩ. Such a device forms a *superconducting nanowire superinductance.*

The capacitance of the central transmission line can be estimated by using the conformal mapping [24] approach as described in appendix B and the shunt capacitance due to the step discontinuity can be estimated as described in appendix D. By experimentally measuring the response of such a resonator and fitting the data with the model described in the previous section, the kinetic inductance of the nanowire can therefore be extracted. Figure 2.6 shows the typical response of a stepped impedance coplanar resonator in which a nanowire superinductor constitutes the central conductor strip .

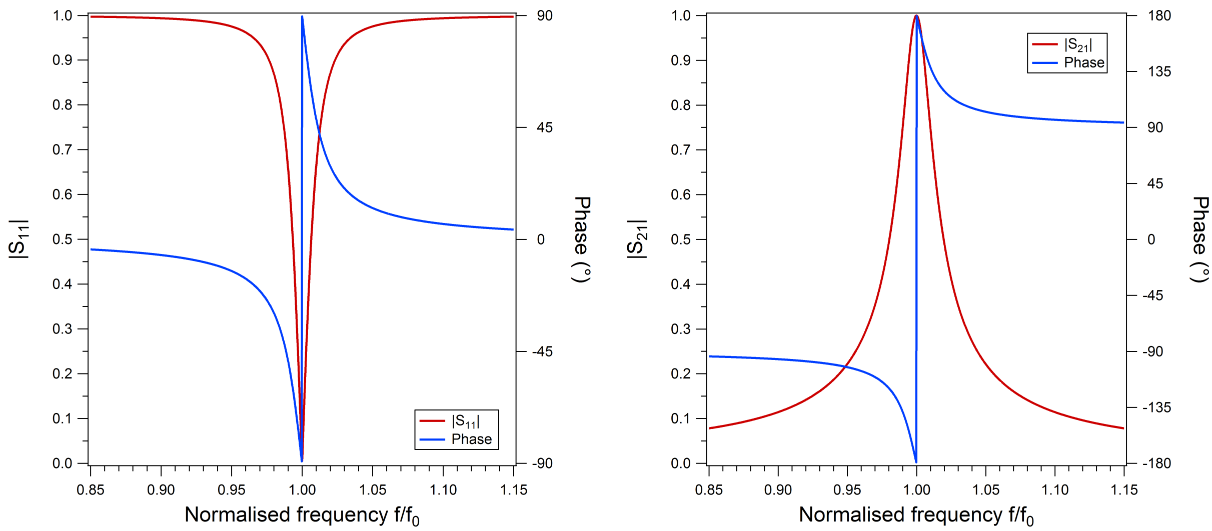

Figure 2.6: Simulated reflected (left) and transmitted (right) magnitude and phase response of a superconducting nanowire superinductance placed in a stepped impedance resonator.

Chapter 3

Experimental Techniques

3.1 Fabrication Techniques

3.1.1 Photolithography

Photolithography is a process used in microfabrication to pattern parts of a thin film or the bulk of a substrate. It uses light to transfer a geometric pattern from a photomask to a light-sensitive chemical (*photoresist*) on the substrate. With a serie of chemical treatments, we can either engrave the exposed pattern on the material underneath the photoresist (*etching*), or a deposite a new material in the exposed pattern (*lift-off*). Figure 3.2 gives an overview of both lift-off and etching processes. It is worth noting that lift-off involves two different photoresists: a so-called *lift-off resist* coated directly on the substrate and a regular photoresist on top. As shown in figure 3.1, the role of the lift-off resist is to form an undercut under the top resist once developed. Once a new layer is deposited, the presence of the undercut allows remover to enter and dissolve the resist. While an undercut also naturally occurs in normal photoresists, the layer is usually too thin for the undercut to be relevant.

Figure 3.1: (Left) With the presence of the undercut, the metal layer (yellow) is not continuous and allows the remover to access the resist. (Right) Without the undercut and lift-off layer, the metal forms a continuous layer on top and remover can't access the resist.

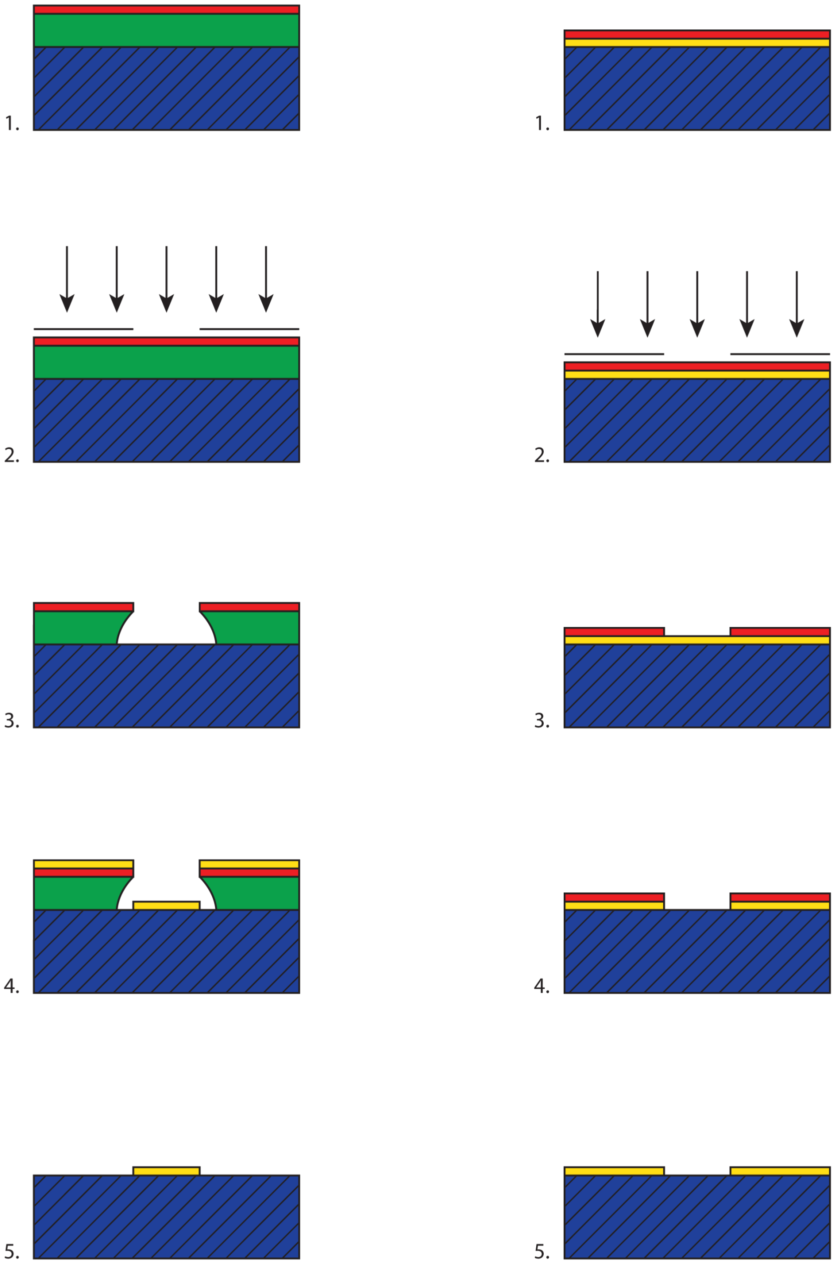

Figure 3.2: (Left) Lift-off process: Lift-off resist (green) and photoresist (red) are spin-coated on a wafer (blue) (1). The resist is then exposed through a mask (2) and developed (3). A metal layer (yellow) is then deposited on top (4). After the wafer is placed in remover, metal remains only where the resist was originally exposed (5). (Right) Etching process: Photoresist is spin-coated on a wafer covered with a thin film (1), the resist is then exposed through a mask (2). After developement, only the unexposed resist remains (3). The uncovered metal is then removed in an etching process (4). Finally, the remaining resist is removed and metal remains in the unexposed area (5).

3.1.2 E-beam Lithography

While photolithography is a fast and cost-effective process, it is however limited in resolution (0.7 µm). To overcome this resolution limit, an e-beam lithography (EBL) system can be used. An EBL system consists of an electron gun, a collimator, magnetic lenses, shutter and deflecting coils [25]. In the electron gun, electrons extracted from a filament are accelerated by an electric field. This stream of electrons is then focused by the collimator and magnetic lenses. The position of the focused electron beam can then be controlled using the deflecting coils. By scanning the beam over the surface of a wafer covered with a resist sensitive to electrons, a pattern can be directly written without the need of any mask.

The wavelength of the electrons, given by de Broglie's relation [26] $\lambda_e = h/p_e$ where p_e is the momentum of the electrons, can be made much smaller than optical wavelengths by controlling the acceleration voltage of the electron gun and therefore allows for the fabrication of features of the order of a few nanometers.

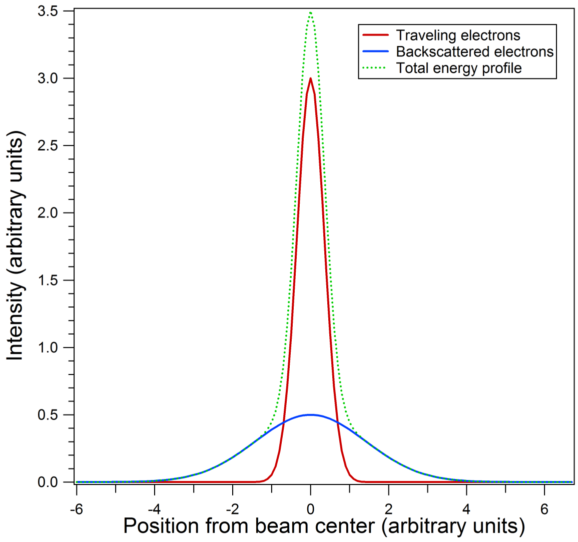

Figure 3.3: Contribution of both traveling and backscattered electrons. The backscattered electrons cover a much larger area than the accelerated electrons.

However, the high energy of the accelerated electrons leads to an unwanted effect known as the *proximity effect*: a lot of the electrons go all the way through the resist into the substrate and are then backscattered back into the resist and expose it. The total exposure profile can be approximated by the sum of two Gaussian curves [27]. As shown in figure 3.3, the backscattered electrons cover an area larger than the intended target and in order to correct this effect, adjustments need to be done. Proximity effect correction is obtained by calculating how long each part of the pattern should be exposed to obtain an even exposure over the whole area.

3.1.3 Physical Vapor Deposition (PVD)

Sputtering

Sputtering is a physical vapor deposition method that involves ejecting a material from a source (the *sputtering target*) onto a substrate. Sputtered atoms ejected from the target have a wide energy distribution and a small fraction are ionised. The sputtered ions can ballistically fly from the target in straight lines and impact energetically on the substrates or vacuum chamber (causing resputtering[1]).

Alternatively, at higher gas pressures, the ions collide with the gas atoms that act as a moderator and move diffusively, reaching the substrates or vacuum chamber wall and condensing after undergoing a random walk. The entire range from high-energy ballistic impact to low-energy thermalized motion is accessible by changing the background gas pressure. The sputtering gas is often an inert gas such as argon. For efficient momentum transfer, the atomic weight of the sputtering gas should be close to the atomic weight of the target, so for sputtering light elements neon is preferable, while for heavy elements krypton or xenon are used. Reactive gases can also be used to sputter compounds. The compound can be formed on the target surface, in-flight or on the substrate depending on the process parameters.

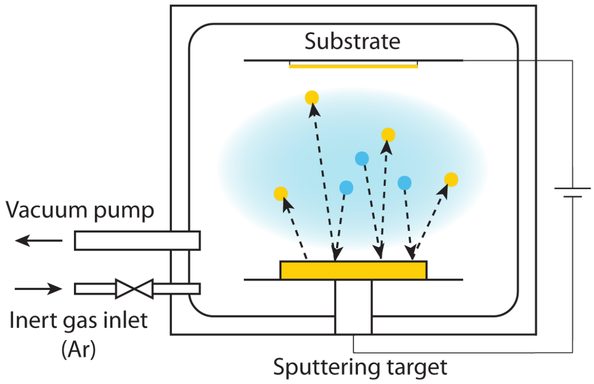

Figure 3.4: Schematic diagram of a typical RF sputtering system. The blue dots represent the Argon ions, the yellow dots the material ejected from the sputtering target.

Electron Beam Physical Vapor Deposition

Electron Beam Physical Vapor Deposition (EBPVD) is a form of physical vapor deposition in which a target anode is bombarded with an electron beam emitted from a charged tungsten filament under high vacuum. The electron beam causes atoms from the target to transform into the gaseous phase. These atoms then precipitate into solid form, coating everything in the vacuum chamber (within line of sight) with a thin layer of the anode material.

[1] Resputtering is the re-emission of the deposited material during the deposition process by ion or atom bombardment.

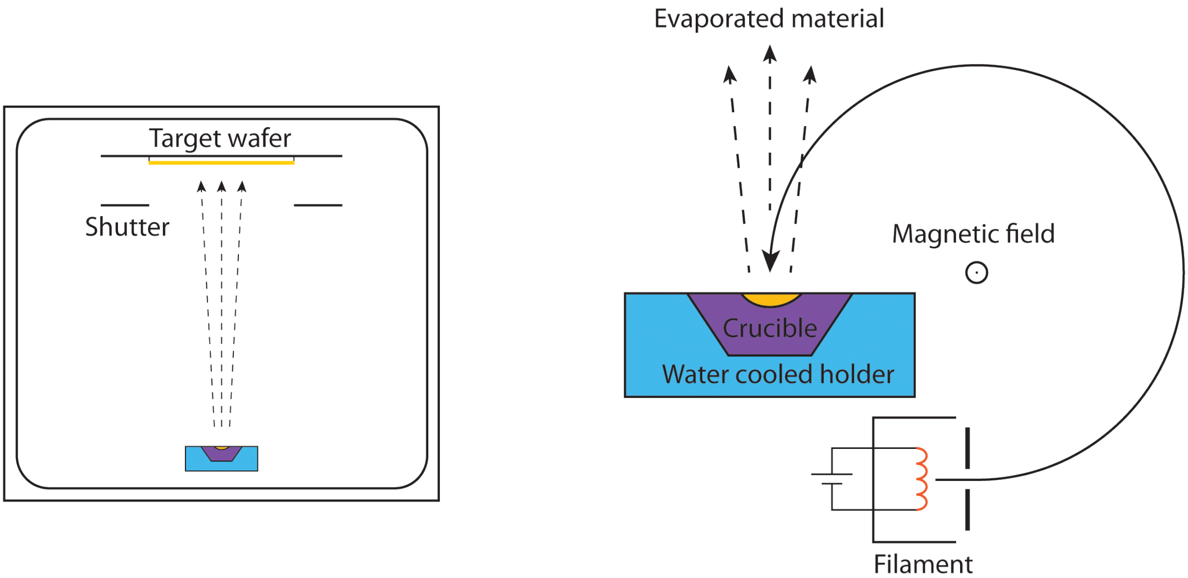

Figure 3.5: (Left) The target wafer is placed in a high-vacuum chamber. Once the material starts evaporating from the source, the shutter is opened and the material starts depositing on the target wafer. (Right) Detailed view of the source. The electrons emitted from the filament are directed by a magnetic field toward a water cooled crucible filled with the desired material. The material heats up in contact with the electrons and evaporates.

3.1.4 Design Considerations

In this work, we have fabricated and measured superconducting NbN nanowire superinductors. As described in section 2.5, the nanowires are placed inside a stepped impedance coplanar resonator in order to be characterised. Due to the large variations in feature dimensions and resolution requirements, it was decided to design a photomask and use a photolithography lift-off process to pattern the large features such as contact pads and ground plane (see figure 3.6). Each chip also contains several areas reserved for various test structures such as Van der Pauw cross structures [28, 29, 30] allowing for on-chip characterisation of the thin NbN film.

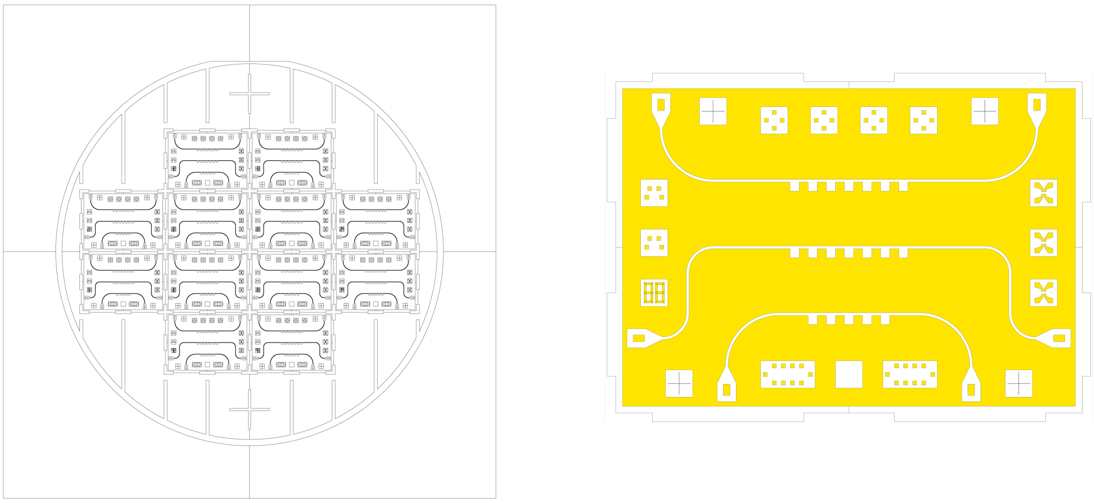

Figure 3.6: (Left) CAD drawing of the photolithography mask used in this work. (Right) Detail of a single chip. The areas marked in yellow will be covered by metal after the lift-off process is completed. In the actual mask, these are the areas allowing the light to go through since in a lift-off process we need to expose the resist where we want to keep the metal.

To keep the design flexible, superconducting coplanar waveguides are patterned using a lift-off EBL process. Each chip is designed around three RF lines, two of them containing a 1 cm long gap in the central conductor to fit a stepped impedance coplanar resonator etched in the underlying NbN layer in a third EBL exposure (see figure 3.7).

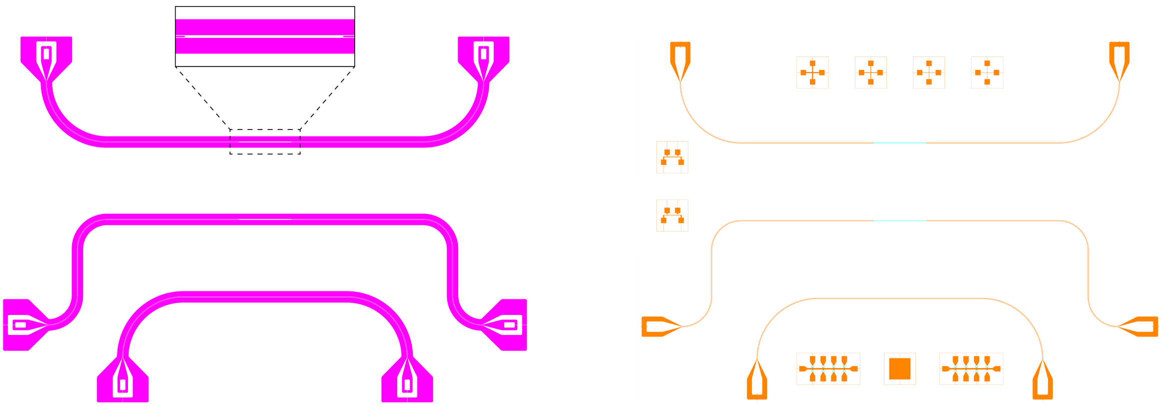

Figure 3.7: (Left) CAD drawing of the EBL pattern for the CPW lines. The insert shows a magnified view of the area for the stepped impedance coplanar resonator. (Right) CAD drawing of the EBL pattern for the NbN etching step to define the test structures and the nanowires. Orange represents the high current exposure (fast but moderately precise) and cyan the low current one (slow but precise).

3.2 Fabrication

All the fabrication steps have been carried out in the cleanroom facilities of the Nanofabrication Laboratory at Chalmers University of Technology. Throughout this section, the reader can refer to appendix A for detailed fabrication recipes.

3.2.1 Wafer and Thin Film Deposition

All the devices were fabricated on 2" 330 µm thick C-plane (0001) Sapphire wafers. On each wafer, twelve 10x7mm chips are fabricated. Prior to any fabrication process, the wafer needs to be cleaned in a bath of warm 1165 remover and then rinsed in isopropyl alcohol (IPA) and water. The first fabrication step then consists of sputtering a 5 nm NbN layer on the wafer in a DCA MTD 450 Sputter.

3.2.2 Photolithography

Then, in the next step, photolithograpy is used to pattern contact pads, ground planes and EBL alignment marks. The wafer is coated with a lift-off resist (LOR3B) and a positive photoresist (S1813). Once exposed in a Suss MicroTec KS MA/BA 6 mask aligner, the wafer is developed in a water-based solvent (MF319) that dissolves only the exposed parts of the resist. After the development, any organic residues from the resist are etched away in an oxygen plasma. The wafer is placed in a Lesker PVD225 ultra high vacuum chamber where a thin metallic trilayer film is evaporated over the whole wafer: 5 nm of Ti, 85 nm Au and finally a 15 nm layer of Pd. The Ti layer is used to obtain a good adhesion between the gold film and underlying NbN film. The top layer Pd is used as a stopping layer to prevent diffusion [31, 32] between Au and the Al film to be deposited in the next step. The excess metal is lifted-off using 1165 Remover.

3.2.3 Electron Beam Lithography

The next step consists of patterning the CPW lines using EBL. The wafer is first cleaned from any residues from the previous step using oxygen plasma again and then coated with a primer (HDMS), a lift-off resist (LOR3A) and a positive electron sensitive resist (UV60). The primer greatly increases the adhesion of the resist on the surface and prevents features about the size of the resist resolution limit from collapsing. The wafer is then exposed in a JEOL JBX-9300FS electron beam lithography machine and developed in MF-CD-26. Once the residues are ashed in oxygen plasma, the wafer is placed in a Plassys electron beam evaporator and a 200 nm layer of Al is deposited. The excess metal is once again lifted-off using 1165 Remover.

The final fabrication step involves patterning the NbN layer and etch the nanowire and test structures. After ashing any resist organic residue, the wafer is coated with a primer (HDMS) and a positive electron sensitive resist (UV60), exposed in a JEOL JBX-9300FS electron beam lithography machine and developed in MF-CD-26. The wafer is ashed and the NbN layer is etched with NF_4 in a Oxford Plasmalab System 100 Reactive Ion Etcher.

3.3 Measurement Techniques

3.3.1 Cryogenics

Measurements involving superconductors rely on our ability to create low enough temperatures. While usually dilution refrigerators are used in order to minimise the noise environment, in order to save both time and resources and allow the quick characterisation of our devices, it was decided to use a custom-made dip stick and measure the devices in liquid Helium where the temperature ($T = 4.2\,\mathrm{K}$) is already well below the critical temperature of NbN ($T_c \simeq 12\,\mathrm{K}$).

3.3.2 DC Measurement Setup

In order to measure the resistivity of the deposited NbN film, a small piece of wafer covered with a thin NbN film of desired thickness is mounted and bonded in a sample holder. The sample holder is then placed in a QuantumDesign Physical Property Measurement System (PPMS). This tool allows for a precise control of the temperature over a wide range (400 to 2 K and temperature sweeps and various types of measurements can be made. In our case, we rely on a four-probe measurement of the resistivity of the film.

Four-probe measurement (also known as *Kelvin sensing*) is an electrical impedance measuring technique that uses separate pairs of current-carrying and voltage-sensing electrodes to make more accurate measurements than the simpler and more usual two-terminal sensing. Separation of current and voltage electrodes eliminates the lead and contact resistance from the measurement.

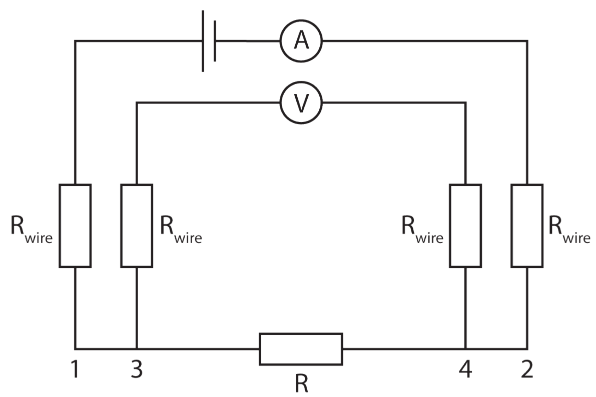

Figure 3.8: Schematic of a four-probe measurement setup. The current is supplied via force connections 1 and 2, these generate a voltage drop across the impedance to be measured according to Ohm's. A pair of sense connections (voltage leads 3 and 4) are made immediately adjacent to the target impedance R, so that they do not include the voltage drop in the force leads or contacts. Since almost no current flows to the measuring instrument, the voltage drop in the sense leads is negligible.

3.3.3 RF Measurement Setup

In order to characterise the RF properties of our devices, the microwave setup shown in figure 3.9 was used. The sample is first mounted and bonded in a custom-made sample box and bonded. The sample box is then mounted on the tail of the dip stick.

The incoming microwave signal is attenuated and filtered to prevent noise from traveling down in the cables. The amount of attenuation is chosen such that the resulting noise temperature matches the noise level in the cryogenic stage. The outgoing microwave signal is amplified by a low noise amplifier (LNA) before exiting the cryogenic stage.

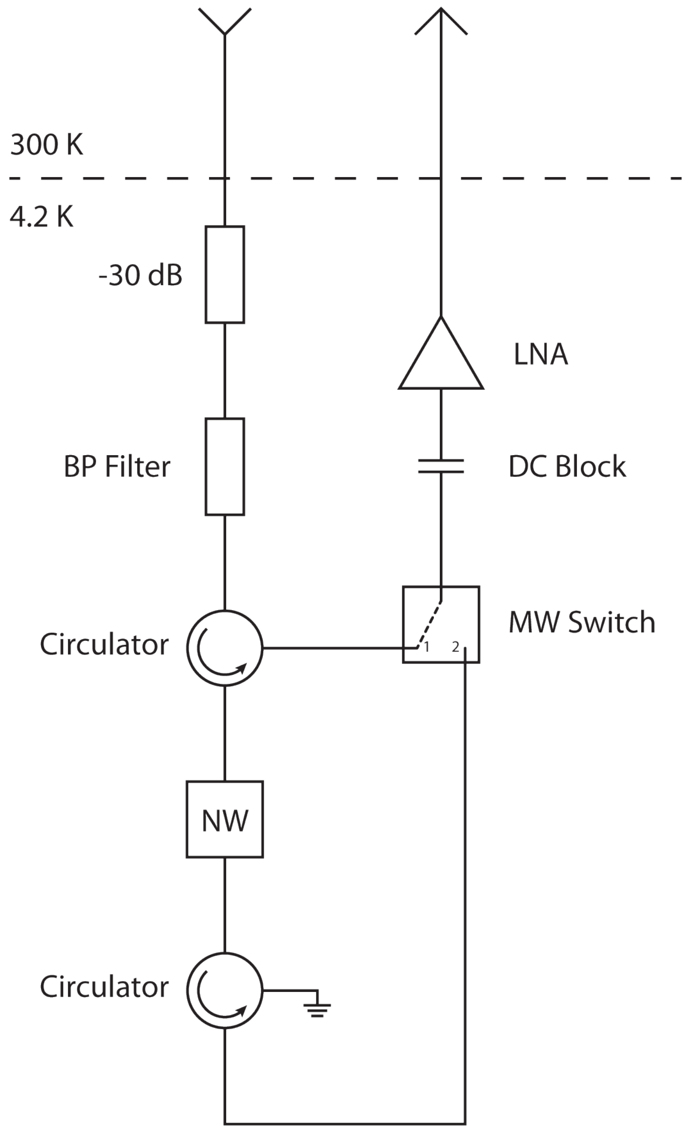

Figure 3.9: Schematic of the micowave measurement setup used. By placing the device (NW) between two circulators and using a microwave switch (MW Switch) both reflection (Switch on position 1) and transmission (Switch on position 2) parameters can be measured in the same setup.

Chapter 4

Results and Discussion

In this chapter, we present the experimental characterisation of the fabricated superconducting nanowire superinductances. We first fabricated thin NbN films and characterised their thicknesses, critical temperatures and normal-state resistances in order to estimate their sheet kinetic inductance. Based on these results and aided by EM simulations using *Sonnet*, we designed, fabricated and characterised our nanowire coplanar waveguide resonators.

4.1 NbN Thin Films

The sputtered thin NbN film determines the properties of our devices. As shown in section 2.2.5, the kinetic inductance is the dominant contribution to the inductance of our nanowires. Therefore, it is important to properly characterise the films in order to ensure reproducibility and to predict the properties of the nanowires.

4.1.1 Surface Characterisation

Film Thickness

In order to optimise the sputtering recipe, originally designed for 140 nm films [33], films of different target thicknesses were sputtered assuming a linear dependance of the thickness with the sputtering time. Films of target thicknesses of 40, 20, 10 and 5 nm were fabricated. After etching away a section of the film, the thickness and surface profile of all fabricated films were measured either using a Tencor P15 surface profiler for the relatively thick films (40, 20 and 10 nm) or a Bruker Dimension 3100 atomic force microscope (AFM) for the 5 nm film. The results are shown in table 4.1 and figure 4.1. While we observe a clear linear dependance for the higher thicknesses, this is not true anymore for lower thicknesses. This can be explained by the abrubt change in the atmosphere composition of the sputtering chamber once the shutter is opened, triggering a faster initial growth. In order to improve these results and enable making even thinner films, one could for example start the sputtering process on a dummy target and present the target wafer after a few seconds of delay once the sputtering conditions are stabilised (by rotating the wafer holder in front of the source).

Table 4.1: Measured film thicknesses compared to desired thicknesses.

Sputtering time	Desired thickness	Measured thickness
120 s	140 nm	-
34.3 s	40 nm	39.2 nm
17.2 s	20 nm	21.6 nm
8.60 s	10 nm	13.2 nm
4.30 s	5 nm	6.90 nm

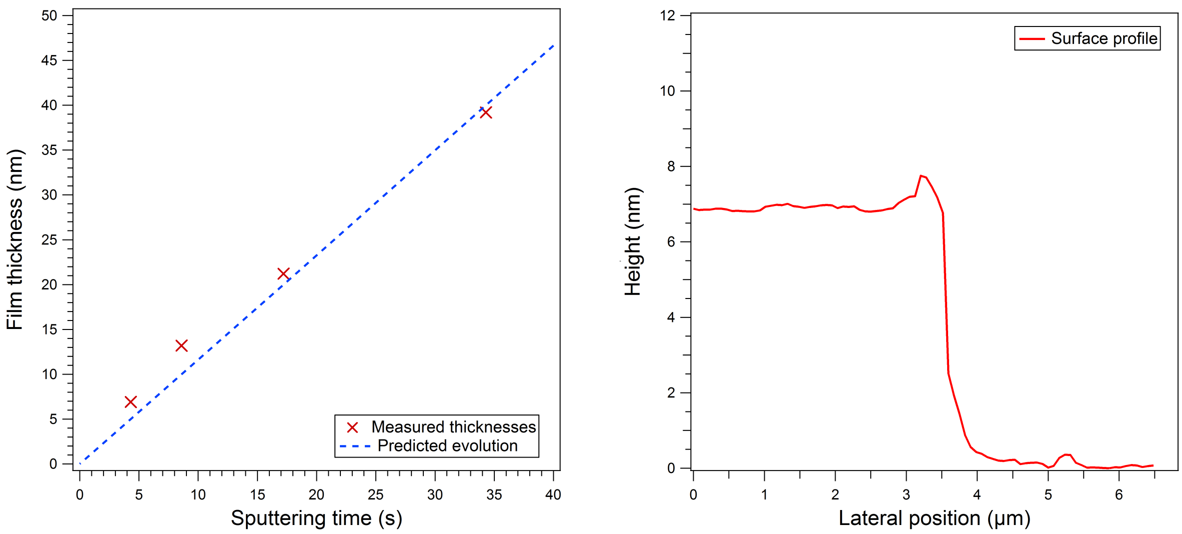

Figure 4.1: (Right) Surface profile of a thin NbN film. The desired thickness was 5 nm, the obtained thickness is 6.9 nm. The edge bump is an artifact caused by the AFM when the scanning needle jumps from a low area to a high area (the scanning direction here is from the right to the left). (Left) Measured NbN film thicknesses as a function of the sputtering time.

Surface Metrology

AFM measurements also allow to investigate the surface properties of a material such as surface roughness, skewness and kurtosis. These parameters, used to describe surfaces, are statistical indicators obtained from many samples. The values presented in table 4.2, extracted from the surface area shown in figure 4.2, are well within what can be found in the literature [34].

Table 4.2: Surface parameters for a 5 nm NbN thin film. The surface skewness is a measure of the symmetry of the profile distribution about the mean line and the surface kurtosis gives an indication of the sharpness of the surface profile.

Parameter	Name	Measured value
R_{RMS}	Root mean squared roughness	0.37 nm
R_{sk}	Skewness	0.558
R_{ku}	Kurtosis	0.236

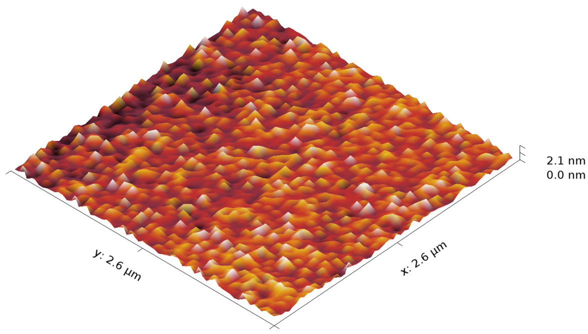

Figure 4.2: AFM picture of the surface of a 5 nm NbN thin film. The measured RMS surface roughness is $R_{rms} = 0.37\,\text{nm}$.

4.1.2 T_c Measurements

In order to determine the critical temperature T_c of a given film, a small fragment of the NbN covered wafer is measured in the setup described in section 3.3.2. T_c for films of different thicknesses have been measured and the results are shown in table 4.3 and figure 4.3. T_c is extracted by calculating the maximum of the derivative of the resistance as a function of the temperature (dR/dT). The decrease of T_c with the film thickness is in agreement with the expected behaviour of superconducting thin films [35, 36, 37, 38, 39].

Table 4.3: Measured critical temperature for various NbN film thicknesses.

Measured thickness	Measured T_c
39.2 nm	12.35 K
21.6 nm	12.10 K
13.2 nm	11.95 K
6.90 nm	11.15 K

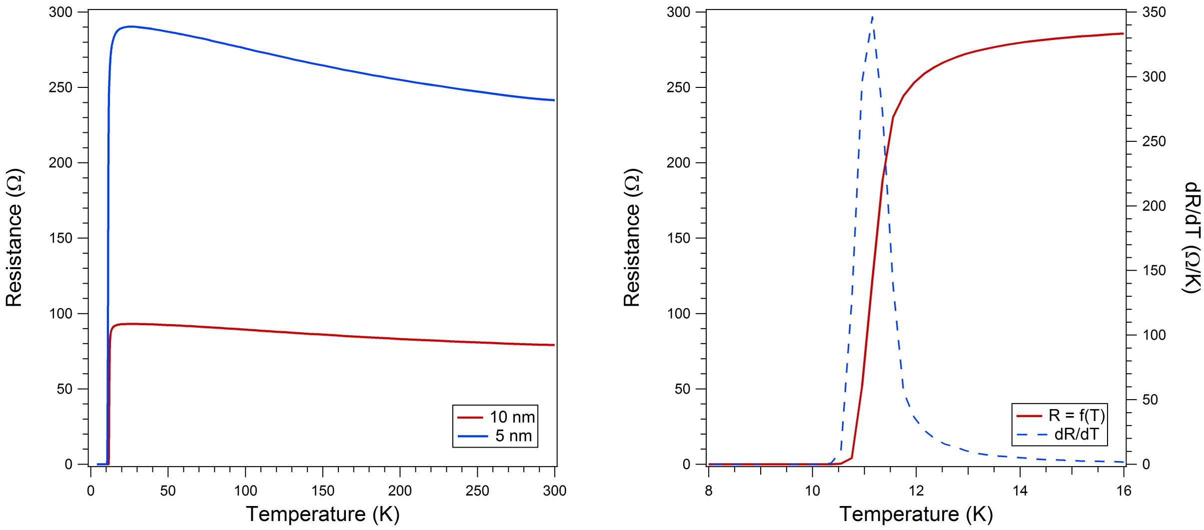

Figure 4.3: (Left) Resistance as a function of temperature for two different NbN thin film thicknesses. (Right) Detail of the transition area for a 5 nm film.

4.1.3 Normal State Resistance and Kinetic Inductance

In order to estimate the kinetic inductance of our films, we need to characterise their normal-state resistance. The measurements shown in table 4.4 were carried out on an AIT CMT-SR2000N four-point probe automated system for measuring resistivity and sheet resistance of wafers and thin metal films. By inserting values for R_n and T_c in equation 2.32, an estimate of the kinetic inductance can be made. We observe that the normal-state resistance (and in turn the sheet kinetic inductance) doubles every time the film thickness is halved. This is again in agreement with the observed behaviour of the normal state resistance of superconducting thin films [40, 41, 42, 43, 44].

Table 4.4: Measured normal state resistance and estimated kinetic inductance for different film thicknesses.

Desired thickness	Measured R_n	Measured T_c	L_k
40 nm	49.7 Ω/□	12.35 K	4.7 pH/□
20 nm	97.8 Ω/□	12.10 K	9.2 pH/□
10 nm	189 Ω/□	11.95 K	18 pH/□
5 nm	359 Ω/□	11.15 K	35 pH/□

4.2 Simulations and Modeling of the Nanowire Coplanar Waveguide Resonator

In order to both validate the theoretical model described in section 2.5 and predict to the response of the fabricated nanowires, extensive simulations have been carried out with the help of the the high-frequency electromagnetic simulation software *Sonnet* [45].

Sonnet offers the possibility to define a material by its surface impedance parameters and can be used to accurately simulate the behaviour of superconductors in the microwave regime. Since in our measurement setup aluminium is in the normal metal state[1], the coplanar waveguide is defined as a 200 nm thick layer of aluminium with finite conductivity ($\sigma = 3.72 \times 10^7\,\mathrm{S\,m^{-1}}$). NbN, however, is superconductive and we assume that the temperature is low enough so that RF losses can be neglected. The material is therefore described as purely inductive with a kinetic inductance of 33 pH/□. Table 4.5 summarises the parameters used for NbN. The structure of the simulated device is shown in figure 4.4.

Table 4.5: ”General metal” parameters used in Sonnet to define the NbN layer.

R_{DC}	R_{RF}	X_{DC}	L_s
0	0	0	33 pH/□

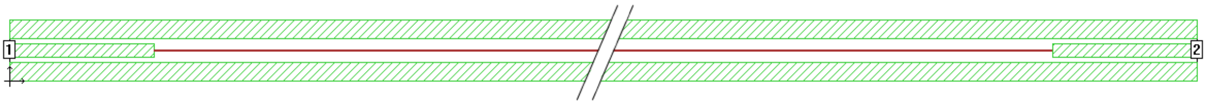

Figure 4.4: Structure of a simulated 100 nm × 1 mm nanowire coplanar resonator in Sonnet. The box is subdivided into 1.0 µm × 0.025 µm cells and closed by lossless top and bottom metal covers.

By fitting the simulation data with the analytical model described in section 2.5, we find that our model is well suited to describe the behaviour of our devices. Both the simulation data and the theoretical model fit are presented in figure 4.5. Table 4.6 presents the obtained fitting parameters and offers a comparison with the parameters simulated in Sonnet and parameters predicted by conformal mapping.

However, while the nanowire parameters are in good agreement with the EM simulation, the obtained value for the shunt capacitance at the impedance step overshoots the predicted value and a closer analysis of the impedance step modeling is required with, for example, an alternative model for the impedance step mentioned in the literature consisting of a T-network with two series inductances and a shunt capacitance [46, 47].

Table 4.6: Fitting parameters from the theoretical model.

Parameter	Conformal mapping	Sonnet	Fitted values
Kinetic inductance	-	33.0 pH/□	34.8 pH/□
Geometrical inductance	$1.37 \times 10^{-6}\,\mathrm{Hm^{-1}}$	$1.60 \times 10^{-6}\,\mathrm{Hm^{-1}}$	-
Capacitance	$4.18 \times 10^{-11}\,\mathrm{Fm^{-1}}$	-	$4.60 \times 10^{-11}\,\mathrm{Fm^{-1}}$
Shunt capacitance	0.13 fF	-	14.7 fF
Total inductance	-	332 nH	349 nH

[1] The critical temperature for aluminium is 1.2 K however our devices are measured at 4.2 K - see section 3.3.3

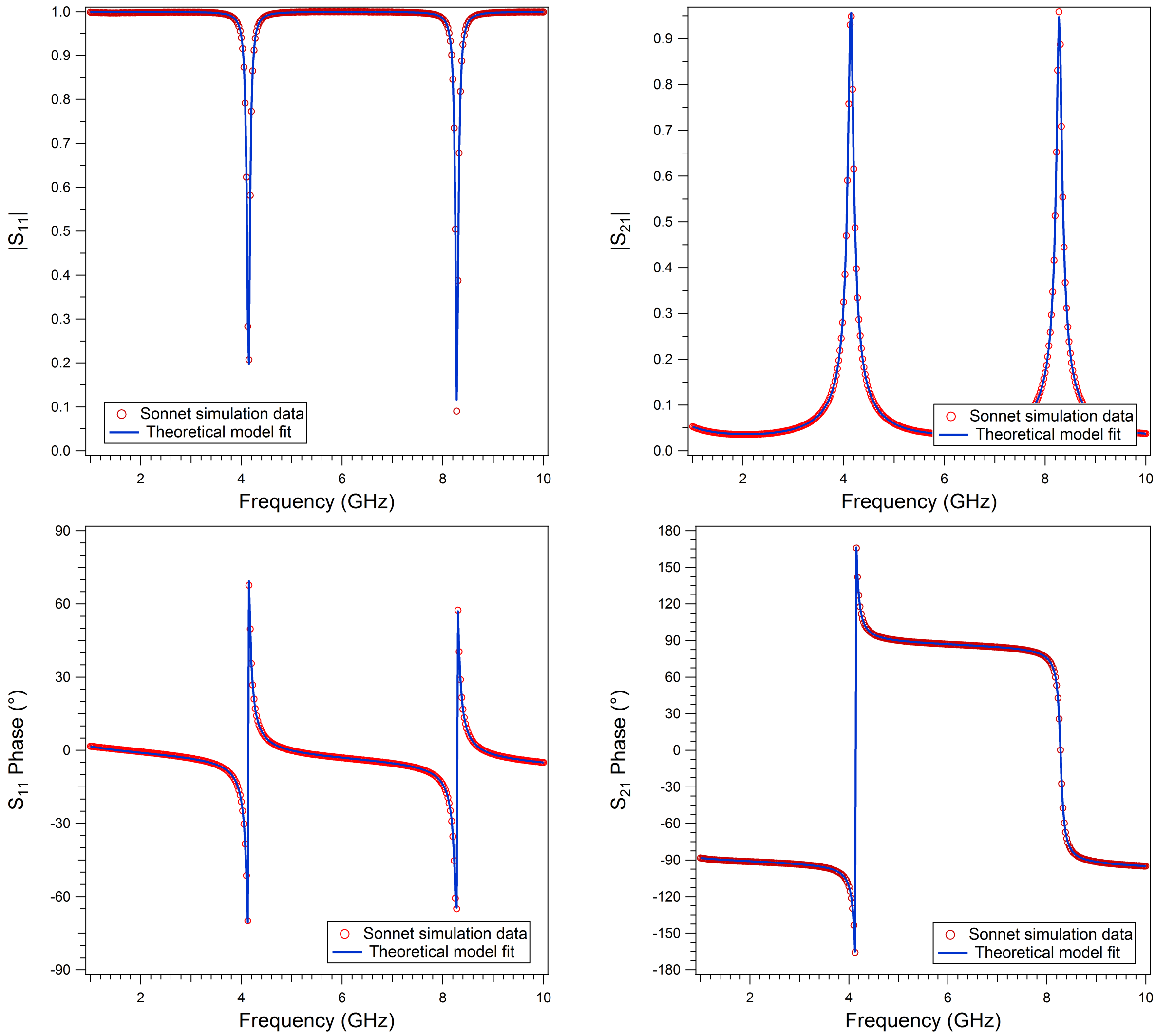

Figure 4.5: Sonnet simulation data plotted and theoretical model fit for both reflection and transmission parameters.

4.3 Microwave Measurements of the Superconducting Nanowire

The fabricated nanowires are measured in the setup described in section 3.3.3. The measured transmissions for a 200 nm × 1 mm nanowire is shown in figure 4.6. The data present many ripples and modes due to the imperfections of both the sample box and the measurement setup. We identify the resonance of the coplanar nanowire resonator by sweeping the input power: since our thin film kinetic inductance is nonlineraly dependent on the current, we expect the resonant frequency of our resonators to vary as a function of the input power.

Unfortunately, the measured device has a resonant frequency outside of frequency range of the maximum gain of our amplifier (4 GHz to 8 GHz); the measurement will therefore present losses that are not related to the resonator itself but due to the measurement setup.

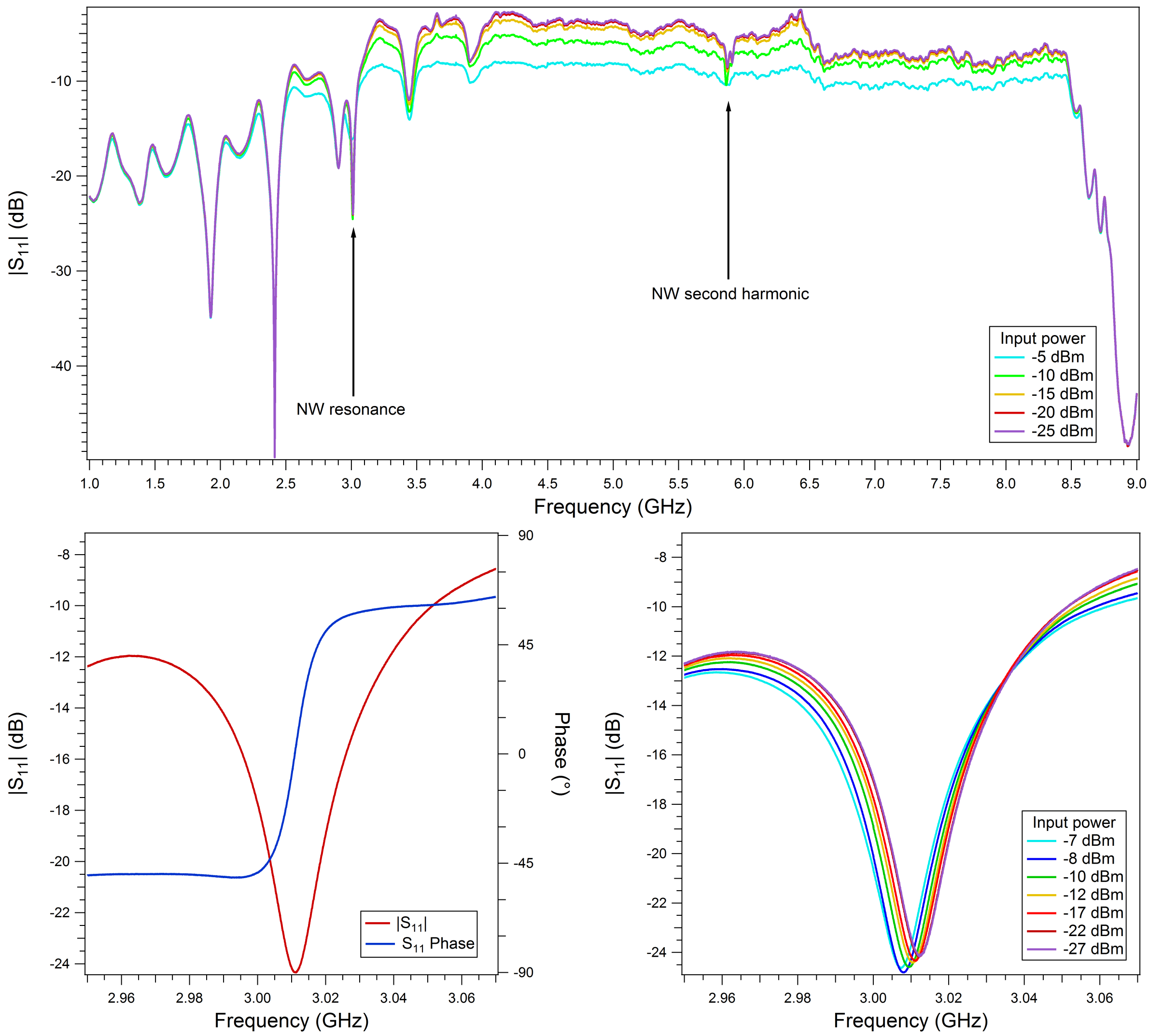

Figure 4.6: (Top) Measured reflection magnitude for different input powers. The resonance and second harmonic are identified as the only peaks where the resonant frequency depends on the power. (Left) Measured reflection magnitude and phase near resonance. (Right) Measured reflection magnitude near resonance for different input powers.

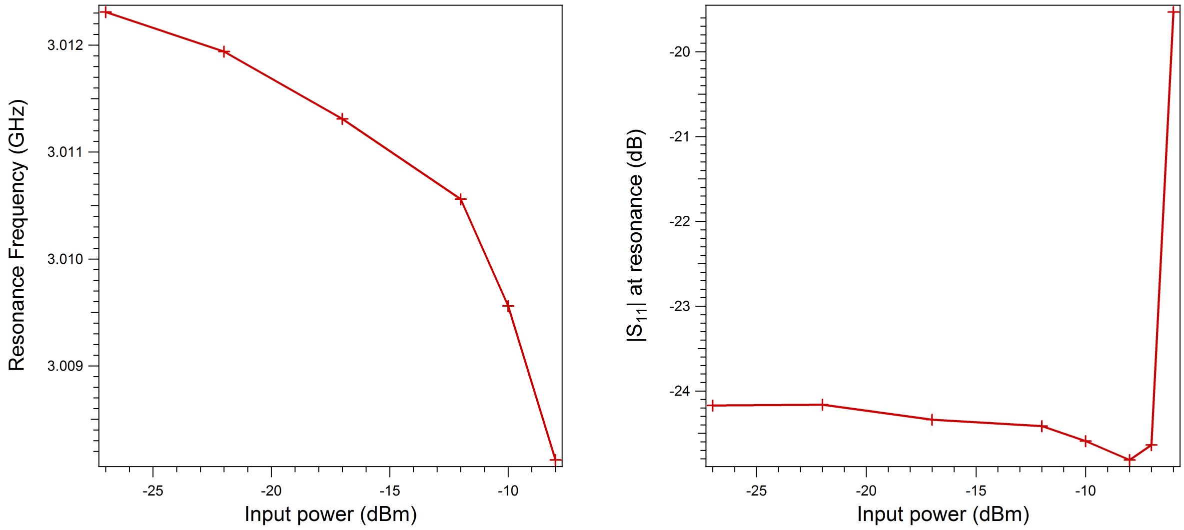

Figure 4.7: (Left) Resonance frequency as a function of input power. (Right) Reflected magnitude at the resonance frequency as a function of input power.

The power dependence of the resonance frequency is shown in figures 4.6 and 4.7. This allows us to extract the critical current density for our thin film. By increasing the power sent to the device, we effectively increase the current going through the wire. Once this current is greater than the critical current of the material, the superconductivity in the nanowire is destroyed and the resonance can no longer be observed.

The input power corresponding to a disappearance of the resonance is $-7\,\mathrm{dBm}$. However the incoming microwave signal is attenuated by $40\,\mathrm{dB}$ before reaching the device (see section 3.3.3). Therefore, the effective power at which the resonance disappears is $P_c = -47\,\mathrm{dBm} = 1.99 \times 10^{-8}\,\mathrm{W}$. This corresponds to a critical current $I_c = 1.95 \times 10^{-5}\,\mathrm{A}$. Since the cross-section area of the nanowire is $S = 6.9\,\mathrm{nm} \times 200\,\mathrm{nm} = 1.38 \times 10^{-11}\,\mathrm{cm}^2$, we have

$$j_c = \frac{I_c}{S} = 1.41 \times 10^6\,\mathrm{Acm}^{-2} \tag{4.1}$$

This value for the critical current density is in agreement with values found in the literature [48].

In order to fit the experimental data and extract the kinectic inductance, we first need to substract the background from our measurements. We assumed a linear background near resonance. Figure 4.8 shows the measured transmission near the resonance once the background is substracted. The descrepancies between the fit and the measured data can be explained by the losses due to the measurement setup. As explained in the previous paragraph, we measure outside of the maximum gain range of our amplifier and therefore these losses aren't modeled by our theoretical fit. However, the fit gives an accurate reading for the inductance and capacitance of our resonator. The fitting parameters are summarised in table 4.7. We immediately notice that we measured an inductance more than twice what we originally estimated from the film properties.

For this result to be explained, we have to take in account both the different sources of error in our measurements and estimates. First of all, while we have established that properties of our thin films are fairly consistent from one fabrication process to another, the properties of the very thin film used in the particular device presented in this section were not characterised. This can lead to a substantial error between the estimated and measured sheet inductance. Moreover, the formula given by equation 2.32 stands only when $\lambda_L \ll \xi$ (extreme anomalous limit). If the extreme anomalous limit isn't verified, some adjustments need to be made to the formula [49]. These parameters haven't been measured on our films, however, values for λ_L and ξ reported in the literature [50, 51] for similar thicknesses lead us to believe that the conditions for the extreme anomalous limit are not met. This, of course, would also lead to some error in the estimated kinetic inductance. Finally, the normal state resistance of the film needs to be characterised at a temperature slightly above T_c. This however was not possible in this work due to limitations in the equipment used. As we can see from figure 4.3, for $T > T_c$ the resistivity of the film increases as the temperature is lowered and measuring R_n at room temperature can lead to a substantial error in the estimated sheet kinetic inductance. As a conclusion, a more systematic characterisation of our thin films needs to be done in order to investigate the discrepancy between estimated and measured values for L_k.

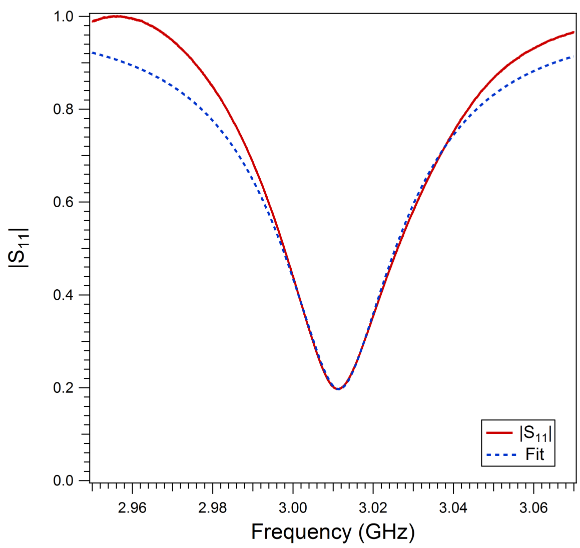

Figure 4.8: Measured reflection at −17 dBm near resonance with substracted background and fit. Kinetic inductance is current dependent, therefore the fitted value is only valid at this power (see figure 4.7).

Table 4.7: Fitting parameters from the theoretical model.

Parameter	Fitted values
Kinetic inductance	78.6 pH/□
Geometrical inductance	1.23×10^{-6} Hm^{-1}
Capacitance	3.50×10^{-11} Fm^{-1}
Shunt capacitance	13.0 fF
Total inductance	787 nH
Resonator wave impedance	4.74 kΩ

Chapter 5

Conclusion and Outlook

In this work we have succesfully fabricated and characterised nanowire superinductances: we measured an inductance of 787 nH; this corresponds to a reactive microwave impedance of $Z = 2\pi f L \simeq 25\,\mathrm{k\Omega}$ at $f = 5\,\mathrm{GHz}$ which is higher than the resistance quantum $R_Q = 1/G_0 = h/4e^2 \simeq 6.5\,\mathrm{k\Omega}$. We have consequently shown that the high kinetic inductance of thin NbN films can be used to fabricate inductors that exhibit an inductance two to three orders of magnitude greater than the geometric inductance of an inductor of the same dimensions. Moreover, we succesfully developed a process that allows for the deposition of very thin NbN films with thicknesses of the order of 5 nm on 2" wafers. We designed step impedance coplanar waveguide resonators where the nanowires were included in order to be characterised, and we have developed a theoretical model for the step impedance coplanar waveguide resonator that accurately fits both EM simulations and measurements.

However, a more careful characterisation of the thin film properties is required. Properties such as the normal-state resistance R_n, the coherence length ξ, the London penetration depth λ_L and the critical temperature T_c need to be systematically characterised for each fabricated film and device. These measurements will help us ensure that the characteristics of our thin films and devices are consistent across different fabrication processes and will give us a better understanding of the physics involved: we worked under the assumption that the Mattis-Bardeen equations, describing the conductivity in a superconductor in the extreme anomalous limit, are valid (i.e. $\lambda_L \ll \xi$), but we need to investigate whether or not this hypothesis holds in our case.

Moreover, in order to reduce the losses in our measurement setup and in our coplanar waveguides, and to reduce the overall noise environment, we need to measure the samples at a much lower temperature ($T \leq 300\,\mathrm{mK}$) in one of the dilution refrigerators available at Chalmers. Finally, the EM modeling of the impedance step must also be better investigated.

While there are still many improvements to be done, these encouraging results open up new perspectives in both quantum information processing and quantum metrology. Our superinductors can be used in combination with Josephson junctions in order to improve existing devices and also to create novel types of quantum electronic devices.

Appendix A

Cleanroom Recipes

A.1 Wafer cleaning

Wafer cleaning	
1165 Remover	60-70°C for 10 min
IPA bath	circulate IPA for 2min
QDR bath	Rinse in water and blowdry with N_2

A.2 Photolithography - S1813 (Lift-off Recipe)

1. HDMS Primer and LOR3B Lift-Off Resist	
Prebake on hotplate	110°C for 1 min
Spin HDMS primer	3000rpm for 5s , $t_{acc} = 1.5\,\mathrm{s}$
Spin LOR3B	3000rpm for 1 min, $t_{acc} = 1.5\,\mathrm{s}$
Hardbake on hotplate	190°C for 5 min

2. S1813 Positive Photoresist	
Spin S1813 resist	3000rpm for 1 min, $t_{acc} = 1.5\,\mathrm{s}$
Softbake on hotplate	110°C for 2 min
Expose pattern	$6\,\mathrm{W/cm^2}$, $t_{exp} = 8.5\,\mathrm{s}$, Lo-vac mode
Develop in MF319	40s
QDR bath	Rinse in water and blowdry with N_2

A.3 Electron Beam Lithography - UV60 (Lift-off Recipe)

1. HDMS Primer and LOR3A Lift-Off Resist	
Prebake on hotplate	100°C for 1 min
Spin HDMS primer	3000rpm for 5s , $t_{acc} = 1.5\,\mathrm{s}$
Spin LOR3A	3000rpm for 1 min, $t_{acc} = 1.5\,\mathrm{s}$
Hardbake on hotplate	180°C for 5 min

2. UV60 Positive Photoresist/EBL Resist	
Spin UV60 resist	3000rpm for 1 min, $t_{acc} = 1.5\,\mathrm{s}$
Softbake on hotplate	130°C for 1 min
Expose pattern	27 µC/cm^2 - 100 kV - 2 nA (70 nA) for small (large) features
Post-exposure bake	130°C for 1 min
Develop in MF-CD-26	1min30s
QDR bath	Rinse in water and blowdry with N_2

A.4 Electron Beam Lithography - UV60

1. HDMS Primer	
Prebake on hotplate	110°C for 1 min
Spin HDMS primer	3000rpm for 1 min, $t_{acc} = 1.5\,\mathrm{s}$
Softbake on hotplate	110°C for 1 min

2. UV60 Positive Photoresist/EBL Resist	
Spin UV60 resist	3000rpm for 1 min, $t_{acc} = 1.5\,\mathrm{s}$
Softbake on hotplate	130°C for 1 min
Expose pattern	27 µC/cm^2 - 100 kV - 2 nA (70 nA) for small (large) features
Post-exposure bake	130°C for 1 min
Develop in MF-CD-26	45s
QDR bath	Rinse in water and blowdry with N_2

A.5 Electron Beam Lithography - UVN2300

UVN2300 Negative Photoresist/EBL Resist	
Prebake on hotplate	100°C for 1 min
Spin UVN2300 resist	3000rpm for 1 min, $t_{acc} = 1.5\,\mathrm{s}$
Softbake on hotplate	100°C for 1 min
Expose pattern	$10\,\mu\mathrm{C/cm^2}$ - 100 kV - 2 nA (70 nA) for small (large) features
Post-exposure bake	110°C for 1 min
Develop in MF-CD-26	45s
QDR bath	Rinse in water and blowdry with N_2

Appendix B

Waveguide Impedance Calculation by Conformal Mapping

In this section, we present the equations used to simulate the characteristic impedance of our coplanar waveguides (CPW). In order to simulate the inductance and capacitance per unit length, the conformal mapping method is used[24]. The electric field lines between the center conductor and the ground planes of the CPW are mapped to the lines of the electric field from a parallel plate capacitor.

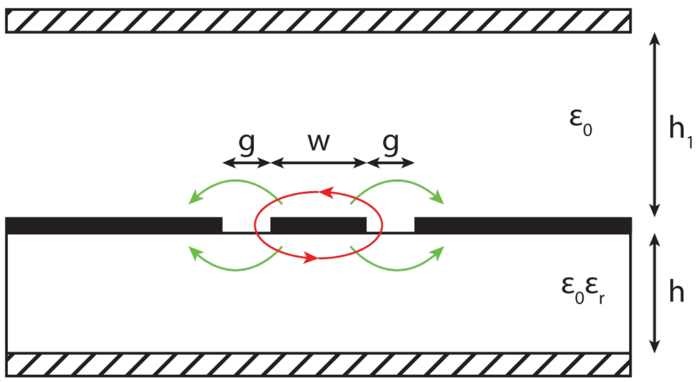

Figure B.1: Cross section of the coplanar waveguide geometry. The superconducting metal (thick black layer) is placed on top of a substrate with effective dielectric constant ϵ_r. The device is placed in vacuum and is surrounded by top and bottom enclosures. h denotes the thicnkess of the substrate and h_1 the distance to the top cover. The electric and magnetig field lines are shown respectively in green and red.

We first calculate C_{vac} and C_1, the capacitance contributions of the vacuum and of the substrate

$$C_{vac} = 2\epsilon_0 \left[\frac{K(k_3)}{K(k_3')} + \frac{K(k_4)}{K(k_4')} \right] \tag{B.1}$$

$$C_1 = 2\epsilon_0(\epsilon_r - 1)\frac{K(k_3)}{K(k'_3)} \tag{B.2}$$

where ϵ_0 and ϵ_r are the vacuum and relative permitivity respectively, and K the complete elliptic integral of the first kind. k_3, k'_3 k_4 and k'_4 are defined by

$$k_3 = \frac{\tanh(\pi w/4h)}{\tanh(\pi(w+2g)/4h)} \qquad k'_3 = \sqrt{1-k_3^2} \tag{B.3}$$

$$k_4 = \frac{\tanh(\pi w/4h_1)}{\tanh(\pi(w+2g)/4h_1)} \qquad k'_4 = \sqrt{1-k_4^2} \tag{B.4}$$

This allows us to define an effective dielectric constant

$$\epsilon_{eff} = 1 + q_2(\epsilon_r - 1) \tag{B.5}$$

where q_2 is a partial filling factors defined by

$$q_2 = \frac{K(k_3)}{K(k'_3)}\left[\frac{K(k_3)}{K(k'_3)} + \frac{K(k_4)}{K(k'_4)}\right]^{-1} \tag{B.6}$$

This enables us to express the phase velocity and characteristic impedance in terms of ϵ_{eff}

$$v_{ph} = \frac{c}{\sqrt{\epsilon_{eff}}} \tag{B.7}$$

$$Z_0 = \frac{1}{cC_{vac}\sqrt{\epsilon_{eff}}} = \frac{60\pi}{\sqrt{\epsilon_{eff}}}\left[\frac{K(k_3)}{K(k'_3)} + \frac{K(k_4)}{K(k'_4)}\right]^{-1} \tag{B.8}$$

Finally, we can express the inductance and capacitance per unit length of the CPW

$$L_{CPW} = \frac{\mu_0}{2}\left[\frac{K(k_3)}{K(k'_3)} + \frac{K(k_4)}{K(k'_4)}\right]^{-1} \tag{B.9}$$

$$C_{CPW} = 2\epsilon_0\epsilon_{eff}\left[\frac{K(k_3)}{K(k'_3)} + \frac{K(k_4)}{K(k'_4)}\right] \tag{B.10}$$

Appendix C

ABCD Matrix of a Transmission Line

By definition of the ABCD matrix, we have for a two-port network with input voltage and current V_1 and I_1, and output volage and current V_2 and I_2

$$\begin{pmatrix} V_2 \\ I_2 \end{pmatrix} = \begin{pmatrix} A & B \\ C & D \end{pmatrix} \begin{pmatrix} V_1 \\ I_1 \end{pmatrix} \tag{C.1}$$

From the telegraph equations[22], the voltage and current at position z along a transmission line can be written as

$$\begin{cases} V(z) = & V^+ e^{-\gamma z} + V^- e^{\gamma z} \\ I(z) = & I^+ e^{-\gamma z} + I^- e^{\gamma z} \end{cases} \tag{C.2}$$

And, by definition, we have

$$Z_0 = \frac{V^+}{I^+} = -\frac{I^+}{I^-} \tag{C.3}$$

where Z_0 is the characteristic impedance of the line. We can rewrite equation C.3 as

$$I^+ = \frac{V^+}{Z_0} \text{ and } I^- = -\frac{V^-}{Z_0} \tag{C.4}$$

This lead to the following expression for equation C.2

$$\begin{cases} V(z) = & V^+ e^{-\gamma z} + V^- e^{\gamma z} \\ I(z) = & 1/Z_0 (V^+ e^{-\gamma z} - V^- e^{\gamma z}) \end{cases} \tag{C.5}$$

These equations stands $\forall z$, we can write them at $z = 0$ and we get

$$\begin{cases} V(0) = & V^+ + V^- = V_0 \\ I(0) = & 1/Z_0 (V^+ - V^-) = I_0 \end{cases} \tag{C.6}$$

This allows us to write the following expressions for V^+, V^-, I^+ and I^-

$$\begin{cases} V^+ = & \frac{1}{2}(V_0 + Z_0 I_0) \\ V^- = & \frac{1}{2}(V_0 - Z_0 I_0) \\ I^+ = & \frac{1}{2}(\frac{V_0}{Z_0} + I_0) \\ I^- = & -\frac{1}{2}(\frac{V_0}{Z_0} + I_0) \end{cases} \tag{C.7}$$

Leading to

$$\begin{cases} V(z) = & \frac{1}{2}(V_0 + Z_0 I_0)e^{-\gamma z} + \frac{1}{2}(V_0 - Z_0 I_0)e^{\gamma z} \\ I(z) = & \frac{1}{2}(\frac{V_0}{Z_0} + I_0)e^{-\gamma z} - \frac{1}{2}(\frac{V_0}{Z_0} + I_0)e^{\gamma z} \end{cases} \tag{C.8}$$

By using Euler's formulas ($\cosh(x) = 1/2(e^x + e^{-x})$ and $\sinh(x) = 1/2(e^x - e^{-x})$), we can write

$$\begin{cases} V(z) = & V_0 \cosh(\gamma z) + Z_0 I_0 \sinh(\gamma z) \\ I(z) = & I_0 \cosh(\gamma z) + \frac{V_0}{I_0} \sinh(\gamma z) \end{cases} \tag{C.9}$$

These last expression can be rewritten as

$$\begin{pmatrix} V(z) \\ I(z) \end{pmatrix} = \begin{pmatrix} \cosh(\gamma z) & Z_0 \sinh(\gamma z) \\ 1/Z_0 \sinh(\gamma z) & \cosh(\gamma z) \end{pmatrix} \begin{pmatrix} V_0 \\ I_0 \end{pmatrix} \tag{C.10}$$

For a line of length l we can therefore write, according to equation C.1

$$ABCD = \begin{pmatrix} \cosh(\gamma l) & Z_0 \sinh(\gamma l) \\ 1/Z_0 \sinh(\gamma l) & \cosh(\gamma l) \end{pmatrix} \tag{C.11}$$

Appendix D

Coplanar Waveguide Step Modeling

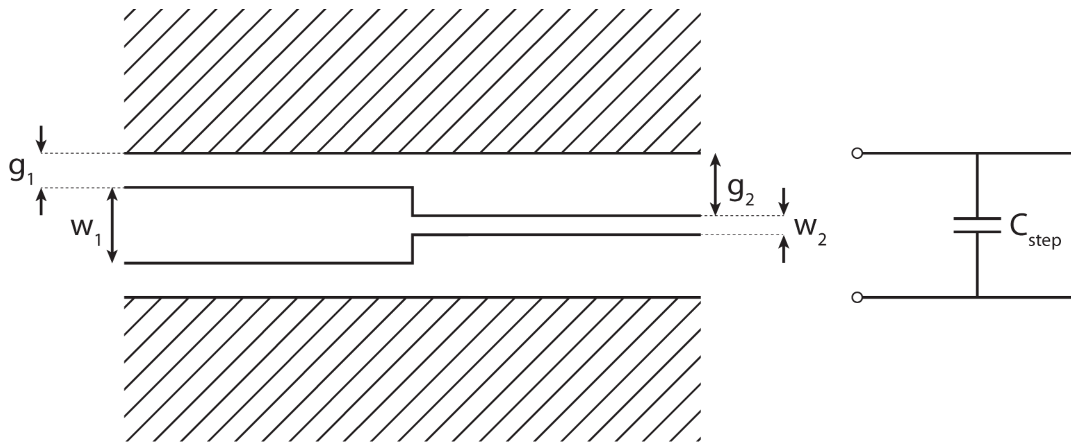

Figure D.1: Coplanar waveguide step discontinuity and equivalent circuit.

The coplanar waveguide step discontinuity has been analysed by C. Sinclair and S. J. Nightingale [52]. The symmetric step change in width of the centre conductor is considered equivalent to a shunt capacitance - this is a reasonable approximation to the CPW step as in the CPW the majority of the field is between the inner and outer conductors with some fringing.

We consider a CPW step discontinuity as shown in figure D.1: the centre conductor abruptly shrinks from w_1 to w_2 while the overall width $(w_i + 2g_i)$ stays constant. We define

$$\alpha = \frac{g_2}{g_1} < 1 \quad \text{and} \quad x_i = \frac{g_i C_{CPWi}}{\epsilon_0} \text{ with } i \in [1;2] \tag{D.1}$$

where C_{CPWi} are the capacitances per length on both sides of the CPW step as derived in appendix B. The shunt capacitance of the coplanar waveguide step derived in [52] is then given by

$$C_{CPW\,step}(\alpha) = \left(\frac{x_1 + x_2}{2}\right)\frac{\epsilon_0}{\pi}\left[\frac{\alpha^2+1}{\alpha}\ln\left(\frac{1+\alpha}{1-\alpha}\right) - 2\ln\left(\frac{4\alpha}{1-\alpha^2}\right)\right] \tag{D.2}$$

Bibliography

[1] M. A. Nielsen and I. L. Chuang. *Quantum Computation and Quantum Information*. Cambridge University Press, Cambridge, 2000.

[2] N. D. Mermin. *Quantum Computer Science*. Cambridge University Press, Cambridge, 2007.

[3] M. H. Devoret and R. J. Schoelkopf. Superconducting circuits for quantum information: An outlook. *Science*, 339(6124):1169–1174, 2013.

[4] V. E. Manucharyan. *Superinductance*. PhD thesis, Yale University.

[5] K. K. Likharev and A. B. Zorin. Theory of the bloch-wave oscillations in small josephson junctions. *Journal of low temperature physics*, 59(3-4):347–382, 1985.

[6] L. I. Glazman M. H. Devoret V. E. Manucharyan, J. Koch. Fluxonium: Single cooper-pair circuit free of charge offsets. *Science*, 326(5949):113–116, 2009.

[7] G. Catelani R. J. Schoelkopf L. I. Glazman M. H. Devoret I. M. Pop, K. Geerlings. Coherent suppression of electromagnetic dissipation due to superconducting quasiparticles. *Nature*, 508:369–372, 2014.

[8] A. J. Kerman. Flux–charge duality and topological quantum phase fluctuations in quasi-one-dimensional superconductors. *New J. Phys.*, 15:105017, 2013.

[9] A. J. Kerman. Metastable superconducting qubit. *Phys. Rev. Lett.*, 104:027002, 2010.

[10] K. H. Onnes. The superconductivity of mercury. *Comm. Phys. Lab. Univ. Leiden*, 251(122), 1911.

[11] L. N. Cooper J. Bardeen and J.R. Schrieffer. Theory of superconductivity. *Phys. Rev.*, 108:1175–1204, December 1957.

[12] W. Meissner and R. Ochsenfeld. Ein neuer effekt bei eintritt der supraleitfähigkeit. *Naturwissenschaften*, 21:787–788, November 1933.

[13] F. London and H. London. The electromagnetic equations of the superconductor. *Royal Society of London Proceedings Series A*, 149:71–88, 1935.

[14] N. W. Ashcroft and N. D. Mermin. *Solid State Physics*. Saunders College Publishing, 1976.

[15] C. J. Gorter and H. Casimir. On superconductivity. *Physica*, 1:306–320, 1934.

[16] J. Zmuidzinas. Superconducting microresonators: Physics and applications. *Annu. Rev. Condens. Matter Phys.*, 3:169–214, 2012.

[17] J. Gao. *The Physics of Superconducting Microwave Resonators.* PhD thesis, California Institute of Technology, 2008.

[18] S. Doyle. *Lumped Element Kinetic Inductance Detectors.* PhD thesis, University of Cardiff, 2008.

[19] A. B. Pippard. An experimental and theoretical study of the relation between magnetic field and current in a superconductor. *Proc. Roy. Soc.*, 216:547–568, 1953.

[20] D. C. Mattis and J. Bardeen. Theory of the anomalous skin effect in normal and superconducting metals. *Phys. Rev.*, 111:412–417, July 1958.

[21] C. P. Wen. Coplanar waveguide: A surface strip transmission line suitable for nonreciprocal gyromagnetic device applications. *IEEE Transactions on Microwave Theory and Techniques.*

[22] D. M. Pozar. *Microwave Engineering 3rd edition.* John Wiley & Sons, New York, 2005.

[23] H. J. Visser. *Antenna Theory and Applications.* John Wiley & Sons, New York, 2012.

[24] N. S. Rainee. *Coplanar Waveguide Circuits, Components and Systems.* John Wiley & Sons, New York, 2001.

[25] S. A. Campbell. *The science and engineering of microelectronic fabrication.* Oxford University Press, 2nd edition, 2001.

[26] L. de Broglie. *Recherches sur la théorie des quanta.* PhD thesis, Ann. Phys. (Paris), 1924.

[27] A. van de Kraats and R. Murali. Proximity effect in e-beam lithography. `http://nanolithography.gatech.edu/proximity.htm`.

[28] L. J. Van der Pauw. A method of measuring the resistivity and hall coefficient on lamellae of arbitrary shape. *Philips Res. Repts*, 13:1–9, 1958.

[29] J. M. David and M. G. Buehler. A numerical analysis of various cross sheet resistor test structures. *Solid State Electronics*, 20:539–543, 1977.

[30] S. Enderling et al. Sheet resistance measurement of non-standard cleanroom materials using suspended greek cross test structures. *Semiconductor Manufacturing, IEEE Transactions on*, 19(1):2–9, 2006.

[31] Kevin Bladh. *Quantum Coherence in the Single Cooper Pair Box.* PhD thesis, Chalmers University of Technology, 2005.

[32] P. Krantz. *Parametrically Pumped Superconducting Circuits.* Licentiate thesis, October 2013.

[33] S. de Graaf. *Fractal Superconducting Resonators for the Interrogation of Two-level Systems.* PhD thesis, Chalmers University of Technology, 2014.

[34] J. M. Meckbach. *Superconducting Multilayer Technology for Josephson Devices : Technology, Engineering, Physics, Applications.* KIT Scientific Publishing, 2013.

[35] A. Shalnikov. Superconducting thin films. *Nature*, 142:74, 1938.

[36] L. N. Cooper. Superconductivity in the neighborhood of metallic contacts. *Phys. Rev. Lett.*, 6:689–690, 1961.

[37] J. E. Mooij M. R. Beasley and T. P. Orlando. Possibility of vortex-antivortex pair dissociation in two-dimensional superconductors. *Phys. Rev. Lett.*, 42:1165–1168, 1979.

[38] A. M. Finkel'stein. Suppression of superconductivity in homogeneously disordered systems. *Phys. B Condens. Matter*, 197(1-4):636–648, 1994.

[39] X.-Y. Bao T.-Z. Han Z. Tang L.-X. Zhang W.-G. Zhu E. G. Wang Q. Niu Z. Q. Qiu J.-F. Jia Z.-X. Zhao Y. Guo, Y.-F. Zhang and Q.-K. Xue. Superconductivity modulated by quantum size effects. 306(5703):1915–1917, 2004.

[40] O. F. Kammerer M. Strongin, R. S. Thompson and J. E. Crow. Destruction of superconductivity in disordered near-monolayer films. *Phys. Rev. B*, 1:1078–1091, 1970.

[41] B. Nease Y. Liu, D. B. Haviland and A. M. Goldman. Insulator-to-superconductor transition in ultrathin films. *Phys. Rev. B*, 47:5931–5946, 1993.

[42] D. L. Shapovalov I. L. Landau and I. A. Parshin. Increase in the superconducting transition temperature of a thin film as a result of the deposition of a normal metal on its surface. *JETP Lett.*, 53(5), 1991.

[43] P. J. Silverman. Superconducting fluctuation effects in the resistive transition of amorphous bismuth films. *Phys. Rev. B*, 16:2066–2071, 1977.

[44] P. J. Silverman. Superconducting fluctuation effects in amorphous-bismuth thin films in the presence of a perpendicular magnetic field. *Phys. Rev. B*, 19:233–237, 1979.

[45] Sonnet Software. High frequency electromagnetic software. `https://www.sonnetsoftware.com/`.

[46] C.-W. Chiu and R.-B. Wu. Capacitance computation for cpw discontinuities with finite metallization thickness by hybrid finite-element method. *IEEE Transactions on Microwave Theory and Techniques*, 45:498–504, 1997.

[47] C.-W. Chiu. Inductance computation for coplanar waveguide discontinuities with finite metallisation thickness. *IEEE Proc. Microw. Antennas Propag.*, 145:496–500, 1998.

[48] A. Semenov A. Engel K. Il'in, M. Siegel and H.-W.Hübers. Critical current of nb and nbn thin-film structures: The cross-section dependence. *Physica Status Solidi*, 2(5):1680–1687, 2005.

[49] J. R. Waldram. *Superconductivity of Metals and Cuprates.* IOP Publishing, 1996.

[50] J. Jesudasan V. Tripathi S. P. Chockalingam, M. Chand and P. Raychaudhuri. Superconducting properties and hall effect of epitaxial nbn thin films. *Phys. Rev. B*, 77:214503.

[51] M. Chand A. Mishra J. Jesudasan V. Bagwe L. Benfatto-V. Tripathi A. Kamlapure, M. Mondal and P. Raychaudhuri. Measurement of magnetic penetration depth and superconducting energy gap in very thin epitaxial nbn films. *App. Phys. Lett.*, 96(7):072509, 2010.

[52] C. Sinclair and S. J. Nightgale. An equivalent circuit model for the coplanar waveguide step discontinuity. *IEEE MTT-S International Microwave Symposium Digest*, pages 1461–1464, September 1992.

CHALMERS UNIVERSITY OF TECHNOLOGY
SE-412 96 Göteborg, Sweden
Telephone: +46 (0)31-772 1000
www.chalmers.se